Advances in the Synthesis and Applications of Self-Activated Fluorescent Nano- and Micro-Hydroxyapatite

Thales Rafael Machado, Jussara Soares da Silva, Eloisa Cordoncillo, Héctor Beltrán-Mir, Juan Andrés, Valtencir Zucolotto, and Elson Longo

Abstract Hydroxyapatite (HA) is the major mineral phase of calcified tissues (i.e., bones and teeth), and the synthetic version of HA has several attractive properties for in vivo applications, ranging from hard tissue repair to drug/gene/protein delivery. In the last decades, HA has been used in combination with lanthanide ions, molecular fluorophores, or inorganic luminescent materials, for the potential use in fluorescence imaging, biosensing and theranostics as well as for the fabrication of optical devices. Recent studies have pointed to the susceptibility of HA to surface and structural defects, which end up impacting its electronic structure and improving its intrinsic fluorescent properties. This chapter highlights the main advances in the synthesis of activator- and dye-free fluorescent nano- and microparticles of HA, in addition to their application in the distinct technological fields and nanomedicine. The available information based on experimental and theoretical approaches about the role of the distinct defects that govern this intrinsic property is also summarized. Lastly, this chapter provides new insights into the design, fabrication and challenges for the further development of HA-based luminescent materials.

T. R. Machado (✉) · V. Zucolotto
GNANO – Nanomedicine and Nanotoxicology Group, Physics Institute of São Carlos, University of São Paulo, São Carlos, SP 89885-000, Brazil
e-mail: tmachado.quimica@gmail.com

T. R. Machado · J. S. da Silva · E. Longo
CDMF – Center for the Development of Functional Materials, Federal University of São Carlos, São Carlos, SP 13565-905, Brazil

E. Cordoncillo · H. Beltrán-Mir
QIO – Inorganic and Organic Chemistry Department, Jaume I University, 12071 Castellón de la Plana, Spain

J. Andrés
QFA – Physical and Analytical Chemistry Department, Jaume I University, 12071 Castellón de la Plana, Spain

C. A. Taft and S. R. de Lazaro (eds.), *Research Topics in Bioactivity, Environment and Energy*, Engineering Materials, https://doi.org/10.1007/978-3-031-07622-0_5

1 Introduction and General Concepts

Calcium orthophosphates (CaPs) are a class of materials abundant in nature that can be found both in geological deposits and as the main inorganic constituents of biological hard tissues [1]. The most important and studied CaP is hydroxyapatite (HA, $Ca_{10}(PO_4)_6OH_2$), known as the primary crystalline phase of bones, teeth and tendons, in a non-stoichiometric version containing various foreign ions and ionic vacancies within the crystal lattice often labeled as bioapatite [2–4]. The synthetic version of HA is strongly timely to biomedical applications because of its compositional flexibility, biocompatibility, bioactivity, non-toxicity, and tailorable biodegradability, granting the synthetic HA the superior ability to interact and bond with surrounding tissues [5–7]. Given these advantages, it is often suggested that HA be applied in reconstructive surgery [8] and bone repair [9–12].

HA at nanoscale has been attracting the attention of researchers in the nanomedicine field due to its potential use in intracellular bioimaging [13, 14] and drug/gene delivery systems for various therapeutic applications, including cancer therapy [15–18]. Besides, HA nanoparticles (NPs) can be applied for theranostic purposes since they are capable of performing diagnosis and therapy functions simultaneously [19]. To these ends, HA particles are combined with distinct contrast agents to improve its imaging capability, for example, for fluorescence imaging procedures. In this process, the fluorescence properties of HA is optimized either by doping the particles with lanthanide ions [20–28] or encapsulating organic fluorophores [29–32], or by combining HA with other luminescent materials in the form of composites [33–36]. On the other hand, the induction of self-activated fluorescence in HA is an exciting research area that avoids the necessity to conduct the aforementioned strategies to obtain satisfactory fluorescent properties and that could create a new range of applications for HA in nanomedicine and other technological fields [37].

The origins of self-activated fluorescence properties in materials are based on the formation of localized energy levels within the band gap region induced by defects, including ionic and interstitial vacancies, impurities, length and angle distortions in atomic bonds, dislocations and stresses in the crystalline lattice, boundaries, cracks, pores, and so on [38, 39]. Pure and stoichiometric HA has a band gap energy (Eg) greater than 5.3 eV, making photoexcitation of electrons from the valence band (VB) to the conduction band (CB) more difficult, with subsequent radiative recombination of electron–hole pairs (e^-–h^+) [40]. However, during the synthesis step it is possible to control the nature and the density of defects, resulting in fluorescent HA (f-HA) particles due to the appearance of new energy levels between the VB and the CB [41–43]. Thereby, this chapter brings an overview of the recent investigations on the synthesis and applications of self-activated fluorescent nano- and micro-HA.

2 Crystallographic Structure of HA

The stoichiometric HA described under the general formula $Ca_{10}(PO_4)_6(OH)_2$ primarily exhibits monoclinic symmetry with space group $P2_1/b$, and after a reversible phase transition from monoclinic to hexagonal polymorph at about 207 °C, it has space group $P6_3/m$ and lattice constants a and c equal to 0.942 and 0.688 nm, respectively [44, 45]. This fact, however, does not imply that natural and biological HA particles, as well as the often-studied synthetic version of HA, adopt a monoclinic pattern. In these cases, the inclusion of foreign ions and the presence of ionic vacancies within the HA crystalline structure typically occur, stabilizing the more disordered and less symmetric hexagonal phase under atmospheric conditions [46].

The crystal structure of hexagonal HA is comprised of a compact assembly of tightly bonded $[PO_4]$ tetrahedral clusters with ten Ca species distributed along two nonequivalent crystallographic sites [47]. At the Ca(I) site, nine oxygen atoms belonging to $[PO_4]$ are coordinated with the Ca atom, originating $[CaO_9]$ clusters. The Ca atoms at this site exhibit a columnar arrangement parallel to the c-axis. On the other hand, the Ca atoms located at the Ca(II) site are coordinated with six oxygen atoms from $[PO_4]$ clusters and one oxygen from the OH group, forming $[CaO_7H]$ clusters (Fig. 1a, b). At the Ca(II) site, the Ca atoms assemble as equilateral triangles lying on opposite sides, where the planes of the triangles are perpendicular to the sixfold screw axis, forming tunnels, i.e., hexagonal channels which are occupied by OH groups along the c-axis (Fig. 1c,d). The O atoms at the OH site are slightly above or below the Ca(II) triangles. A partial occupancy of 50% at the OH site takes place, and the OH groups are arranged in a disordered fashion, in which the heat-to-tail (OH OH OH…) and tail-to-head (HO HO HO…) arrangements alternate along the channel [46].

The peculiar structure of HA supports tremendous lattice distortions, which in turn allow the occurrence of ionic substitutions within several crystallographic sites by species with various sizes and valence states. These substitutions can originate the Ca-deficient (Ca/P < 1.67) or Ca-rich (Ca/P > 1.67) non-stoichiometric versions of HA rather than the stoichiometric ones (Ca/P = 1.67) [50]. The bioapatite present in bone and tooth mineral illustrates this structural flexibility—it is defective and non-stoichiometric due to the high availability of elements in the body that allow the incorporation of various ionic species within the crystalline lattice, including F^-, Cl^-, Na^+, K^+, Fe^{2+}, Zn^{2+}, Sr^{2+}, Mg^{2+}, CO_3^{2-}, and citrate ions [51]. Therefore, in order to avoid structure charge imbalance, coupled ionic substitutions and/or vacancy generation (e.g., Ca^{2+} and OH^- vacancies) typically occur when ions with different charges from those observed for the groups that comprise the HA structure are incorporated.

One of the most relevant substituting species in HA is CO_3^{2-}. The carbonatation of HA is energetically favorable, with a formation energy of -518.7 kJ.mol^{-1}, causing the spontaneous incorporation of CO_3^{2-} groups into the HA lattice [52]. In bioapatite, the CO_3^{2-} content varies from 2 to 8 wt% depending on the age. In most cases, the synthesis of HA leads to the carbonated version of HA. When CO_3^{2-} groups are accommodated at the OH^- site (A-type substitution), a V_{OH} vacancy is generated.

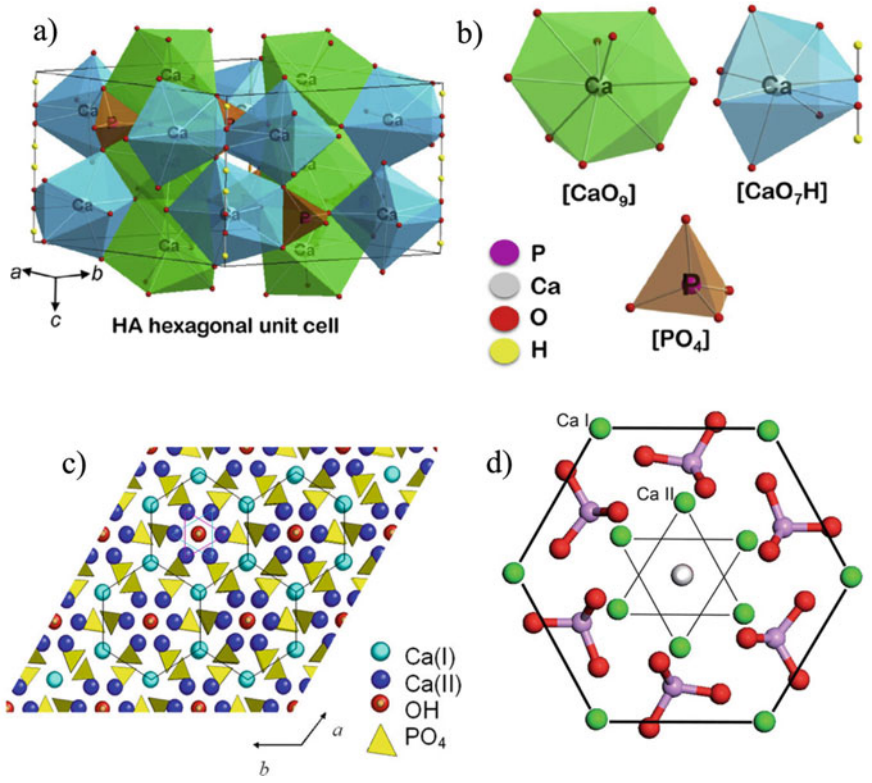

Fig. 1 Representations of **a** HA hexagonal unit cell, and **b** [PO_4], [CaO_9], and [CaO_7H] polyhedra showing the possible upward and downward orientations for OH^- groups. Reprinted with permission from Ref. [37]. **c** HA structure along the *c*-axis, where black lines represent the hexagonal networks formed by Ca(I) sites, while cyan and magenta triangles connect staggered Ca(II) sites with different height in relation to the *c*-axis. Reprinted with permission from Ref. [48]. **d** Illustration of one single hexagonal building unit of the HA structure projected in the [001] direction. Reprinted with permission from Ref. [49]

Meanwhile, the substitution of the PO_4^{3-} group by CO_3^{2-} (B-type substitution) is compensated by the formation of V_{Ca} and V_{OH} vacancies [53]. A concomitant substitution of the OH^- and PO_4^{3-} groups by CO_3^{2-} can also occur (the so-called AB-type substitution). Furthermore, the incorporation of CO_3^{2-} into the HA lattice can be charge-compensated by the introduction of foreign ions, such as Na^+, K^+, NH_4^+ and H_3O^+, depending on the precipitation conditions [54].

Single or multiple substitutions and vacancies, including those associated with CO_3^{2-}, significantly affect the lattice parameters, the degree of structural order at long and short ranges, the crystallization mechanisms, and the exposed surfaces, which in turn change, for instance, the biodegradability, bioactivity, biocompatibility and mechanical resistance of the material, allowing researchers to tailor the behavior of HA in biological environments according to the desirable biomedical application

[55]. These structural and compositional changes conducted during the synthesis can also modify the electronic structure and charge distribution of HA nano- and microparticles, leading to self-activated f-HA with improved emission properties.

3 Synthesis of Luminescent HA

Wet chemical methods are the most promising approaches for the fabrication of f-HA nano- and microparticles with controlled crystallinity, morphology, and size, as well as for the introduction of several types of defects. The manipulation of the density and chemical nature of the defects is crucial to obtaining f-HA, thus requiring an appropriate choice of the synthesis methodology and experimental parameters. There is a large variety of reported techniques based on chemical precipitation, synthesis from natural bio-resources, hydrothermal-assisted precipitation, and sol–gel method, which will be addressed below.

3.1 Chemical Precipitation

Among the various methods to obtain f-HA, chemical precipitation in aqueous solution is the easiest explored one. This synthesis route is based on the fact that HA is a sparingly soluble salt in neutral and alkaline aqueous solutions and that all intermediates will eventually be converted into HA phase [18]. Calcium hydroxide, calcium nitrate and calcium chloride are generally employed as precursor reagents for Ca^{2+}, whereas orthophosphoric acid, diammonium hydrogen phosphate and disodium hydrogen phosphate are commonly used as precursor reagents for PO_4^{3-} [56]. Typically, the controlled addition of one reagent to another is made under stirring, and the resulting milky suspension is aged for several hours, or immediately recovered. The aging step is crucial to converting CaP precursor phases into HA, and its duration depends on the other synthesis parameters employed, mainly temperature. At room temperature, HA is obtained only after a few hours, whereas above 90 °C this phase stabilizes almost instantaneously [57]. The aged suspension is then washed, filtered or centrifugated, dried and crushed into a powder.

Shape and size distribution of HA particles as well as their composition and crystallinity are significantly affected by the parameters adopted during the chemical precipitation procedure, including concentration, pH value and rate of addition of precursor solutions, temperature during synthesis, duration of the aging step, and atmosphere [58]. These properties influence not only the osteoconductivity, biocompatibility, bioactivity, and biodegradability of HA [59], but also its intrinsic fluorescence since the density of several types of optically active surface, interface and structural defects is also affected.

Chemical precipitation at room temperature renders poorly crystalline, calcium-deficient AB-type carbonated f-HA particles when $(NH_4)_2HPO_4$ and $Ca(OH)_2$ or

CaO are used as PO_4^{3-} and Ca^{2+} sources, respectively, in air atmosphere and with an aging step of 15 h [60]. In these cases, the f-HA particles have similar rounded shape with average particle size of 60 ± 20 nm. On the other hand, well-crystallized f-HA particles with tunable sizes and shapes, including hexagonal microprisms (0.7–2.5 μm × 70–200 nm), nanorods (300–600 nm × 40–80 nm), rice-like NPs (50–60 nm × 12–25 nm), microplates and microneedles (0.5–5.5 μm × 30–200 nm) and needle-like NPs (200–700 nm × 20–50 nm), are obtained at 90 °C in an aging period of 2 h by varying the rate of addition of $(NH_4)_2HPO_4$ solution to $Ca(NO_3)_2{\cdot}4H_2O$ solution (0.15, 7.00 or 600.00 mL/min) as well as the pH value adopted (4.5–5.0 or 9.5–10.0), as summarized in Fig. 2 [39]. The long- and short-range structural order of f-HA particles as well as their compositions vary with these synthesis conditions, ranging from calcium-deficient HA ($Ca_{10-x}(HPO_4)_x(PO_4)_{6-x}(OH)_{2-x}$ ($0 < \times < 1$)) in more acidic conditions to compositions closer to those of stoichiometric HA in alkaline conditions.

3.1.1 Heat Treatment Steps

The self-activated fluorescence of chemically precipitated HA is significantly affected by posterior heat treatment steps, leading to a large increase of its emission intensity compared to untreated particles. For instance, f-HA nanorods (300–600 nm × 40–80 nm) exhibit enhanced fluorescence intensity when obtained via chemical precipitation at 90 °C followed by annealing at 350 or 400 °C in air atmosphere [61]. For rounded carbonated calcium-deficient f-HA NPs (60 ± 20 nm) synthesized at room temperature, the ideal heat treatment setup was found to be between 400 and 450 °C [60]. Furthermore, calcium-deficient carbonated f-HA NPs obtained in simulated body fluid (SBF) solution at room temperature can also be made highly fluorescent by annealing at 400 °C [62].

3.1.2 Preparation of Doped f-HA

Doping of HA can improve its in vitro and in vivo behavior, including bioactivity, adsorption of proteins/growth factors, and cell proliferation capability, through the incorporation of several ionic substituents into the HA lattice, as recently reviewed by Tite and colleagues [55]. For instance, Mg^{2+}-doped (5 wt.%) f-HA nanorods (18–31 nm × 9–19 nm) were obtained by microwave-assisted precipitation at room temperature, leading to a large increase in fluorescence intensity [63]. In another study, Sr^{2+}-doped f-HA with enhanced fluorescence properties was prepared by chemical precipitation of HA at 100 °C followed by aging for 24 h at room temperature and a posterior sintering step at 1000 °C for 2 h [64]. Subsequently, an ion exchange process of Ca^{2+} by Sr^{2+} was carried out by suspending the HA powder in strontium nitrate solution for 5 h. The fluorescence intensity was further improved by soaking the Sr-doped f-HA in SBF up to 32 days due to the incorporation of CO_3^{2-} impurity.

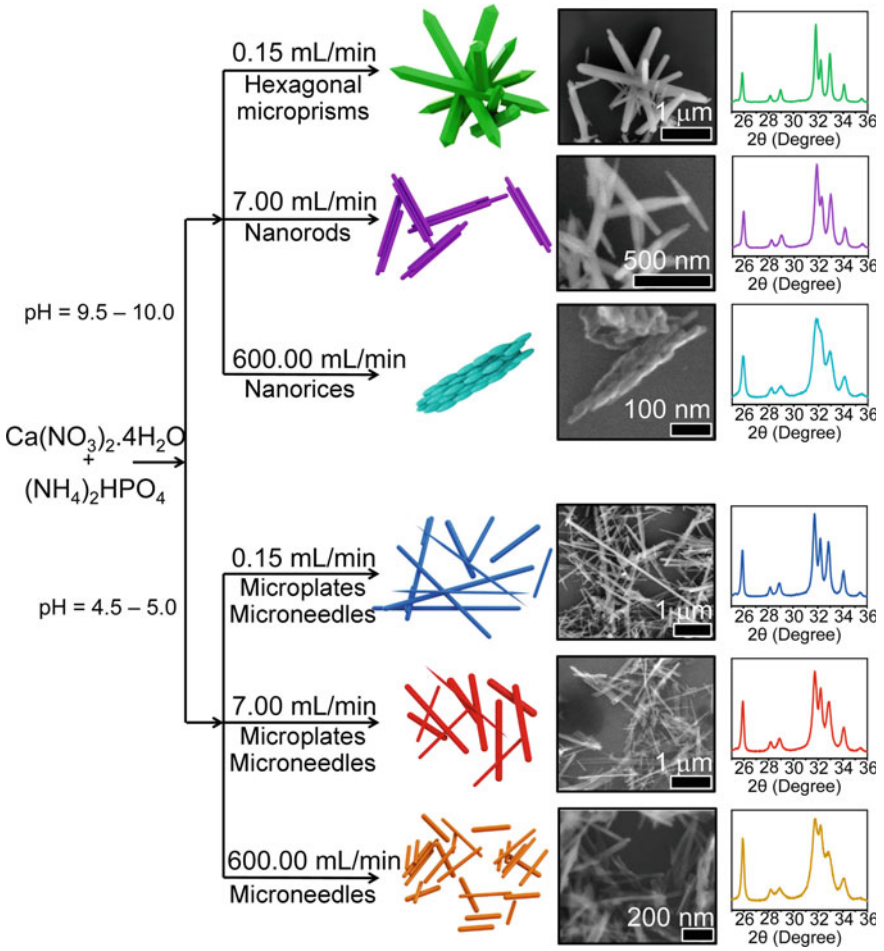

Fig. 2 Nano- and microparticles of f-HA obtained by chemical precipitation at 90 °C and their corresponding XRD patterns. The particle shape, size, degree of crystallinity and composition can be modified by controlling the pH value adopted and the rate of addition of phosphate solution to calcium solution. Reprinted with permission from Ref. [39]

3.1.3 Synthesis of f-HA-Based Composites

The preparation of composite materials containing f-HA nano- and microparticles can be made in order to enhance the intensity of f-HA emission or tune the emission profile of the final composite material. In both cases, charge transfer mechanisms at the interfaces generated between the materials are the main responsible for these behaviors. In this sense, Arul and colleagues [65] prepared polyvinyl alcohol (PVA)/f-HA nanocomposites via microwave-assisted precipitation of f-HA for 30 min at room temperature. The procedure comprised the mixing of 0.5 g of dried powders with

0.0%, 0.5%, 1% and 1.5% of PVA followed by their deposition onto Ti substrate. The authors observed that the intensity of the blue fluorescence of f-HA (centered at 441 nm, $\lambda_{exc} = 254$ nm) increased as a function of PVA concentration. In another study, da Silva et al. [66] synthesized a defect-related luminescent composite with tunable emission colors via in situ precipitation of α-$AgVO_3$ (AV) in f-HA aqueous suspensions in f-HA/AV molar ratios between 1:1 and 1/32:1. Figueroa-Rosales and colleagues [67] developed f-HA/multi-walled carbon nanotube (MWCNT) composites by chemical precipitation followed by ultrasound bath and microwave radiation. A post-heat treatment step at 250 °C for 6 h was also conducted to improve the fluorescence properties of the final composite materials.

3.2 Synthesis from Natural Bio-Resources

The usage of biowastes such as animal bones, fish scale, eggshell and oyster shell among others to prepare HA-based materials is considered a potential waste management strategy to reduce the environmental impact from animal agriculture and food industry [50]. These abundant by-products with no economic value can thereby be converted into value-added products. In addition, HA-based materials obtained from biogenic sources can be well-accepted by living organs due to their physicochemical similarities with bioapatite [56]. In general, HA can be fully extracted from biowaste, acting as the entire source of CaP, or obtained by the reaction of a phosphate precursor with Ca^{2+} extracted from a biogenic source.

Kumar and Girija [68] reported the preparation of flower-like f-HA nanostructures from biowaste by the complexation of Ca^{2+} from processed and purified eggshell powder (mainly $CaCO_3$) with ethylenediamine tetra-acetic acid (EDTA). The Na_2HPO_4 solution was slowly added to the Ca-EDTA complex, and the resulting solution was then stirred for 30 min, with subsequent pH adjustment to 13. Afterwards, the mixture was irradiated in a microwave oven for 10 min, washed and dried, forming the f-HA precipitate. It was observed that the photoluminescent flower-like NPs were composed of 100–200 nm wide and 0.5–1 μm long leaves with Mg^{2+} and CO_3^{2-} impurities inherited from the eggshells.

In another approach, Goloshchapov and coworkers [69] initially extracted CaO from bird's eggshells through an annealing procedure at 900 °C/2 h, and subsequently mixed the product with distilled water at 100 °C to produce $Ca(OH)_2$. Then, a titration was conducted with H_3PO_4 at room temperature with controlled pH in the 7–9 range (step of 0.5) to obtain distinct levels of CO_3^{2-} incorporation. Finally, the precipitate was filtered and dried at 400 °C/1 h to form carbonated f-HA with low crystallinity. Porous rod-like NPs with diameter of ~20 nm and length of ~50 nm were prepared following this methodology, with the best fluorescence intensity being achieved at pH = 8–9 due to the high incorporation of CO_3^{2-} impurity into the f-HA lattice in this pH range.

Sinha and coworkers [70] used a simple heat treatment to obtain f-HA from *Labeo Rohita* fish scales acting as a CaP source. After cleaning the scales with boiling water

for 20–25 min followed by 24 h of water immersion at room temperature, the scales were dried, crushed and calcinated at distinct temperatures (from 400 to 1000 °C) for 1 h. The best fluorescence emission intensity was achieved at 800 °C, temperature at which impurities such as collagen and other proteins are more efficiently eliminated without a significant conversion of f-HA into β-TCP phase with poor luminescence.

3.3 Hydrothermal-Assisted Precipitation

Zhang and colleagues [71] pioneered the preparation of HA particles with improved fluorescence by using citrate ions (Cit^{3-}) in hydrothermal treatments, being this approach one of the most explored so far. In a typical route, an aqueous solution containing $Ca(NO_3)_2.4H_2O$ precursor and hexadecyltrimethylammonium bromide (CTAB) surfactant is mixed with another solution containing $(NH_4)_2HPO_4$ precursor and Cit^{3-} in a Ca^{2+}:Cit^{3-} ratio of 1:1, which is maintained at 180 °C for 24 h. The f-HA particles with distinct morphologies are obtained depending on the pH adopted for the synthesis (Fig. 3). Short nanorods crystallize in more alkaline environments, with lengths ranging from 50 to 70 nm at pH = 9.0 and 120 nm at pH = 7.0 (Fig. 3a, b). In contrast, in acidic environments more complex structures are formed, including self-assembled bur-like microspheres at pH = 5.0 (Fig. 3c, d) and microflowers at pH = 4.5 (Fig. 3e, f), with diameters of 7–9 and 10 mm, respectively, and microsheets at pH = 4.0, with lengths of 0.7–1 mm (Fig. 3g, h).

It could be noted that the presence of Cit^{3-} plays an important role in the final morphology of f-HA due to the formation of the citrate-Ca^{2+} ion chelating complex, which ends up retarding the preferential growth of HA along the *c*-axis direction. In this specific work, the presence of this complex led to short HA nanorods instead of the nanowires typically observed in hydrothermal synthesis at pH ≥ 7.0 without Cit^{3-} addition [71, 72]. As also reported by Lin's group [73], the Cit^{3-}-based hydrothermal route can also be used to prepare Sr^{2+}-substituted f-HA (f-SrHA) microrods and microsheets at shorter reaction times (0.5 and 1 h, respectively) or self-assembled microspheres at larger reaction times (6–48 h) with distinct sizes and crystallinities using $Sr(NO_3)_2$ as Sr^{2+} source and at an Sr^{2+}:Cit^{3-} ratio of 1:2.

Further studies have focused on the determination of the ideal precursors to obtain highly fluorescent f-HA particles via Cit^{3-}-based synthesis. In this sense, Jiang and colleagues [74] demonstrated that the presence of both Cit^{3-} and NH_4^+ ions in the initial solution originated efficient luminescent centers in f-HA NPs through the combination of Na_3Cit and $(NH_4)_2HPO_4$ or $(NH_4)_3Cit$ and Na_2HPO_4 precursors, while no significant radiative emissions were detected when employing Na_3Cit and Na_2HPO_4 or only $(NH_4)_2HPO_4$. Furthermore, Cheng and colleagues [75] observed that by increasing the amount of $(NH_4)_3PO_4{\cdot}3H_2O$ in the initial mixture of $(NH_4)_3PO_4{\cdot}3H_2O$/$Na_3PO_4{\cdot}12H_2O$ precursors it was possible to enhance the fluorescence emission because of the higher concentration of NH_4^+ ions in the hydrothermal reaction.

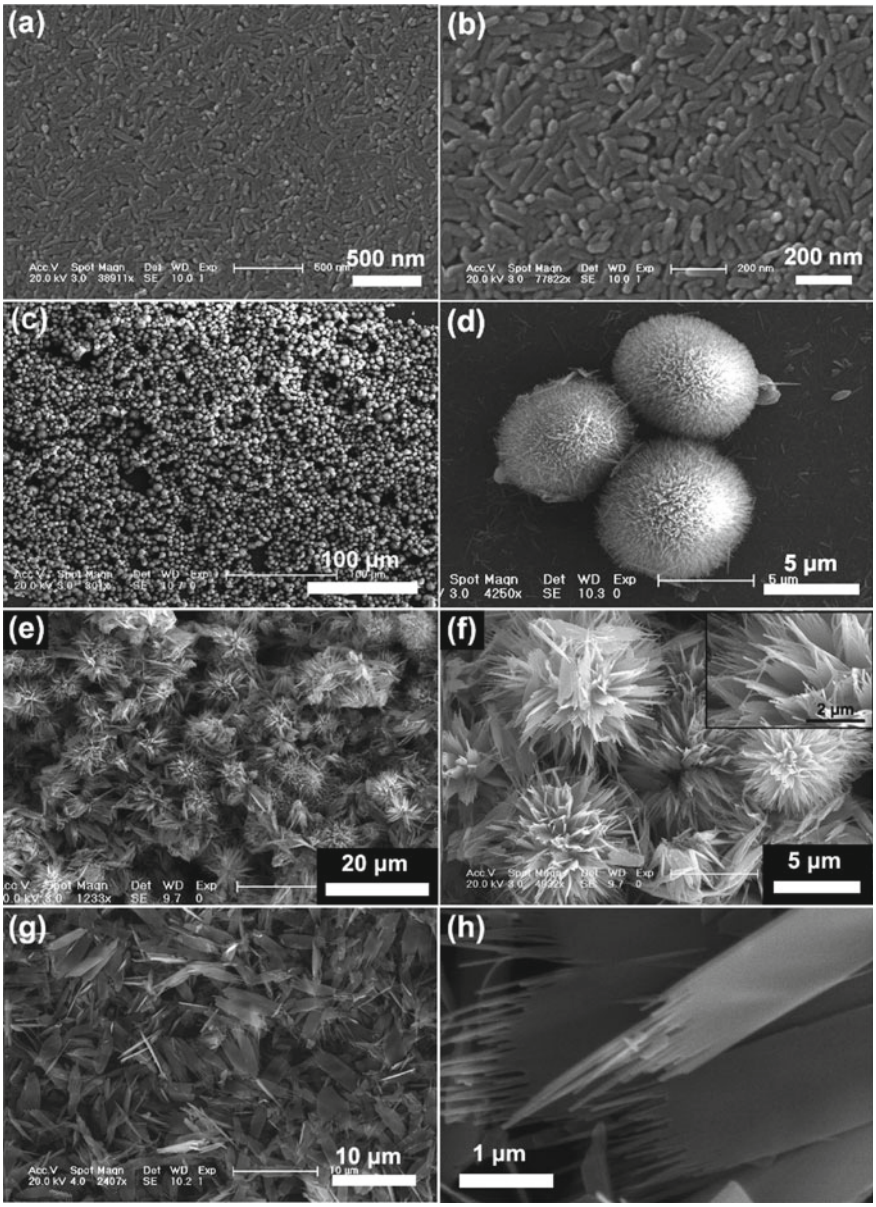

Fig. 3 Scanning electron microscopy (SEM) images of f-HA particles obtained via hydrothermal treatment in the presence of Cit^{3-} showing distinct morphologies resulting from changes in the pH value during the reaction. **a, b** Short nanorods, pH = 7.0; **c, d** bur-like microspheres, pH = 5.0; **e, f** microflowers, pH = 4.5; and **g, h** microsheets, pH = 4.0. Reprinted with permission from Ref. [71]

The usage of distinct precursors during the Cit^{3-}-based synthesis of f-HA can also affect the duration of the reaction and bring novel properties to the final material. For instance, shorter reaction times of 3 h at 175 °C and pH = 9 enabled the formation of f-HA nanorods with length of around 100 nm in the presence of polyethylene glycol (PEG) instead of CTAB surfactant, as reported by Yang et al. [76]. On the other hand, Wang and colleagues [77] prepared f-HA nanorods doped with Tb^{3+} by the addition of $Tb(NO_3)_3.5H_2O$ and demonstrated the effect of Cit^{3-} and Tb^{3+} on the crystal phase, morphology and fluorescent properties of f-HA, evidencing that the radiative emissions can be tuned from blue to green by changing the initial amount of Cit^{3-} precursor. Additionally, Li and colleagues [78] synthesized aptamer-capped f-SrHA nanorods doped with Gd^{3+} by using $Gd(NO_3)_3.6H_2O$ precursor and successfully obtained HA NPs with both self-activated fluorescence and paramagnetic properties.

Although it is known that Cit^{3-} plays a key role in the improvement of the fluorescent properties of HA, other methodologies based on hydrothermal-assisted precipitation without Cit^{3-} precursor also lead to a final material with superior optical properties, as recently demonstrated by Huerta and colleagues [79]. In another work, Park et al. [80] prepared f-SrHA microspheres with Sr/[Ca + Sr] molar ratios of 0, 0.25, 0.50 and 1.00 using poly(aspartic acid) (PASP) as a template. The self-assembled PAPS structure was formed via peptide bonds between $–COO^-$ and $–NH_3^+$ groups of two different L-aspartic acid (L-Asp) precursor molecules. It was found that another $–COO^-$ group of L-Asp monomer interacts with Ca^{2+}, forming a chelate. These chelates act as sites for the nucleation and growth of f-SrHA, leading to the occurrence of fluorescent carbon impurity sites. According to the authors, the size, morphology and surface of the particles can be tuned depending on the reaction time and the amount of both L-aspartic acid (L-Asp) and Sr^{2+} precursor, which in turn forms weaker chelates with carboxyl groups than Ca^{2+} ions.

3.4 Sol–Gel Method

Deshmukh and coworkers [81] synthesized self-activated f-HA NPs with a modified sol–gel method using triethylamine (TEA) or acetylacetone (ACA) as stabilizing agents and water or dimethyl sulfoxide (DMSO) as solvents. In this procedure, calcium chloride was first dissolved in DMSO and H_3PO_4 was introduced into the former solution by a dropwise addition followed by the influx of TEA or ACA and pH adjustment to 10. The obtained gel was washed, dialyzed, and dried at room temperature. Comparatively, the authors added TEA or ACA stabilizing agent to the H_3PO_4 solution, which was in turn added dropwise to the calcium chloride aqueous solution. It was found that the best setup to obtain highly fluorescent HA was with DMSO and ACA. Under these conditions, it was possible to obtain thin rod-like f-HA NPs (62.5 nm in length × 6.2 nm in diameter) exhibiting a hydrodynamic size of 57 ± 10 nm and a zeta potential of 2.12 mV. When the synthesis was conducted without stabilizing agents, the NPs consisted of rod-like microparticles (1.42 μm × 0.29 μm).

Although f-HA particles can efficiently load and deliver therapeutic biomolecules (i.e., antibiotics and chemotherapy drugs) in a controllable manner, some researchers have focused on the improvement of their loading capacity by combining them with mesoporous silica (mSi) to fabricate core–shell nanostructures. Yang and coworkers [82] used a modified Pechini sol–gel process to prepare spherical mSi NPs covered by a uniform f-HA layer. Briefly, a water/ethanol mixture, citric acid, CTAB and PEG were added to an acidic solution (pH 2–3) containing both Ca^{2+} and PO_4^{3-} sources followed by the addition of mSi NPs previously prepared by base catalyzed sol–gel method using a tetraethyl-orthosilicate (TEOS). The diameters of mSi@f-HA NPs were around 200–400 nm, whereas the surface area, average pore diameter and pore volume were 1348 m^2g^{-1}, 2.44 nm and 0.92 cm^3g^{-1}, respectively. These values were several times higher than those typically reported for f-HA (e.g., 20–90 m^2g^{-1} of surface area [83, 84]) and had the potential to load superior quantities of biomolecules. Moreover, spherical mSi NPs covered by f-HA nanorods (f-HA@mSi) were also obtained by a similar approach, but using f-HA nanorods previously prepared via Cit^{3-}-assisted hydrothermal treatment instead of the soluble salts containing Ca^{2+} and PO_4^{3-} species [72].

In another study, f-HA nanorods covered by a thin shell of mSi were obtained by base catalyzed sol–gel synthesis of mSi in a dispersion of f-HA nanorods prepared by Cit^{3-}-containing hydrothermal treatment [85]. The thickness of the mSi layer of f-HA@mSi nanorods was controlled by the amount of TEOS used (from ~9 nm to ~28 nm), as illustrated in Fig. 4. The final f-HA@mSi NPs were 68 × 100 nm long and 30 × 63 nm wide and exhibited a surface area, an average pore diameter and a pore volume of 104.6–223.1 m^2g^{-1}, 3.649–3707 nm and 0.1664–0.4763 cm^3g^{-1}, respectively—values that varied depending on the thickness of the mSi layer.

4 Self-Activated Luminescence

Generally, the self-activated luminescence emission spectrum of f-HA particles obtained by wet methods is composed of a broad band profile centered at 430–530 nm (2.88–2.34 eV) and covering a large part of the UV and visible regions of the electromagnetic spectrum. To achieve such luminescence, f-HA samples are often excited at $\lambda_{exc} = 325–415$ nm (3.81–2.99 eV) in the near-UV region. However, depending on the synthesis and processing approaches, the proposed emission centers responsible for the observed fluorescence are different, and both the emission and the excitation wavelengths can be red-shifted towards less energetic regions by tunning the defects present in the f-HA structure [37].

Considering that neither Ca^{2+} nor PO_4^{3-} ions emit fluorescence by themselves and that a small amount of energy is often employed to excite f-HA particles in comparison with the calculated values for the optical band gap energy (E_g) of pristine HA (E_g = 4.60–5.67 eV [40, 86, 87]) as well as those experimentally determined (5.41–5.78 eV [61, 88]), the fluorescence in HA has its origin most likely related to the e^-–h^+ pair recombination encompassing localized energy states between the VB and

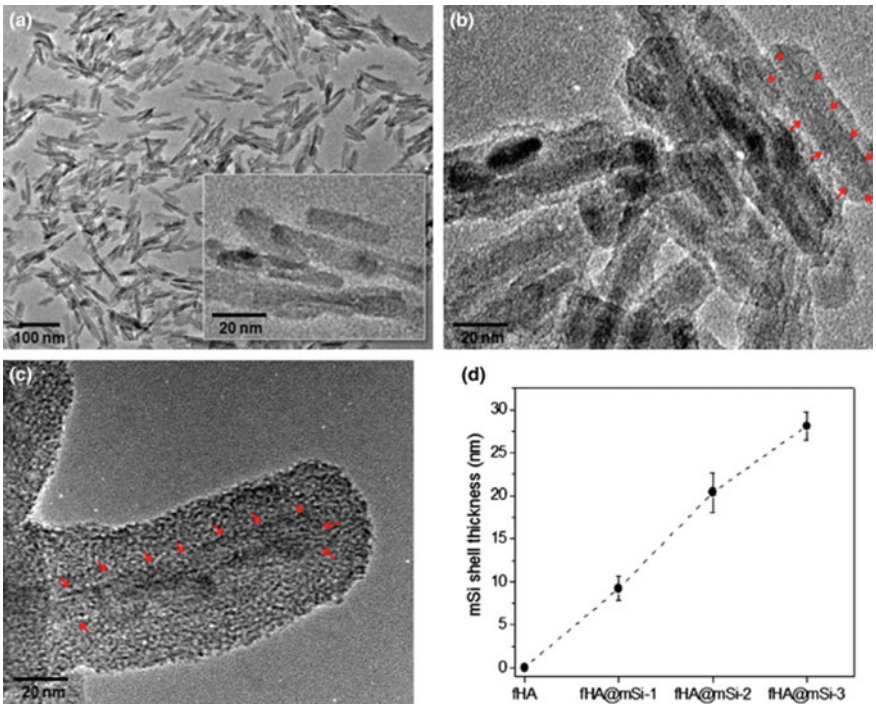

Fig. 4 Transmission electron microscopy (TEM) images of **a** f-HA nanorods, and **b, c** f-HA nanorods covered by a small and a large layer of mSi, respectively. **d** Calculated values of mSi thickness for samples prepared using 50 uL (fHA@mSi-1), 100 uL (fHA@mSi-2), and 150 uL (fHA@mSi-3) of TEOS. Reprinted with permission from Ref. [85]

the CB, i.e., in the forbidden gap of HA. In general, ionic vacancies (e.g., V_{Ca}, V_{OH}, and V_O vacancies in PO_4^{3-}), ionic substitutions and impurities (e.g., CO_3^{2-}, H_2O and NH_4^+), and interstitials (e.g., H_i) in the HA structure induce distortions at both long and short ranges with changes in its lattice parameters, volume, and electronic energy states (an example is shown in Fig. 5a, b), behavior that was evidenced by several theoretical studies based on first-principles calculations [41, 42, 87, 89–93] and experimental approaches [53, 54]. These phenomena have the potential to give rise to several luminescent centers, as a redistribution of electrons takes place between extended and localized electronic levels exhibiting both acceptor- and donor-like characters, consequently leading to self-activated fluorescence in HA in the near-UV and visible regions of the electromagnetic spectrum.

In the case of HA synthesized via wet approaches, the nano- and microparticles are non-stoichiometric and often possess significant density of CO_3^{2-} point defects inside the crystalline lattice when obtained in air atmosphere. As previously mentioned, these groups that substitute PO_4^{3-} and/or OH^- are mainly stabilized by the formation of ionic vacancies (V_{Ca} and V_{OH}), the incorporation of H_2O molecules and the occurrence of other ionic substitutions (HPO_4^{2-}, Na^+,

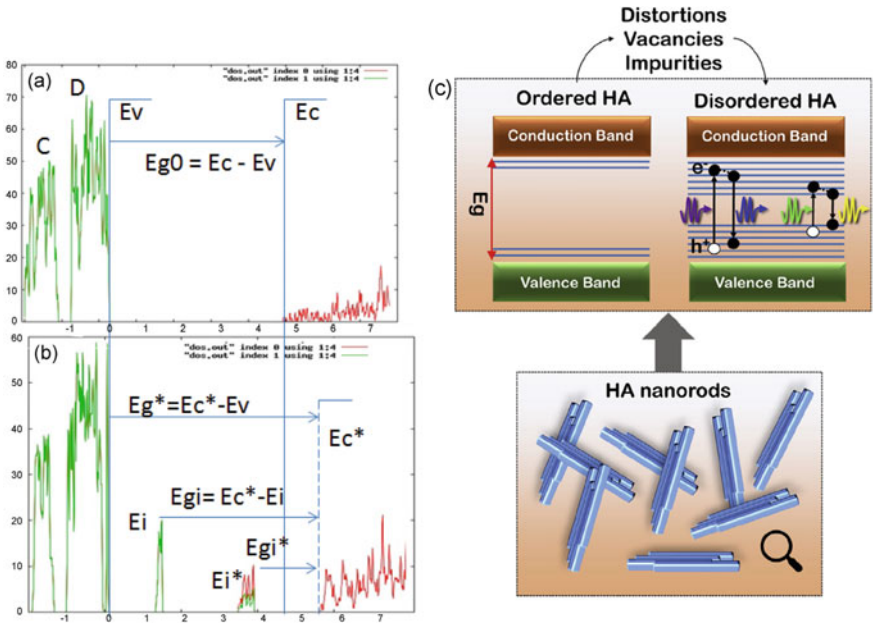

Fig. 5 Electronic energy levels in the band gap region of HA. **a** Density of states (DOS) image of stoichiometric HA, and **b** DOS image of HA containing point defects that lead to localized states within the forbidden zone with potential for fluorescence emissions in near-UV and visible regions. Legends: energy levels occupied by electrons are represented in green, whereas those represented in red are unoccupied. C and D = upper peaks of the VB; Ev = top of the VB; Ec = bottom of the CB; Ei and Ei* = fully occupied and half-occupied localized energy states arising from V_O vacancies in PO_4^{3-} and V_{OH} vacancies, respectively. Reprinted with permission from Ref. [41]. **c** General scheme based on the broad band model for the occurrence of self-activated fluorescence in HA nanorods obtained by chemical precipitation. In an ideal ordered HA system, the energy levels in the forbidden zone are minimized. However, the presence of defects causes a higher disorder in the HA system, thus allowing a radiative recombination of e^-–h^+ pairs between the VB and the CB. Reprinted with permission from Ref. [37]

NH_4^+, H_3O^+), depending on the parameters adopted during synthesis [46, 54]. The V_{OH} vacancies can also occur due to lattice disorder, as proposed by Pasteris and colleagues [94]. Furthermore, HPO_4^{2-} can incorporate into the HA lattice in more acidic environments, leading to calcium-deficient HA containing both V_{Ca} and V_{OH} vacancies [54]. These defects also have profound impact on the atomic arrangement of HA since they promote structural defects as well as distortions in bond lengths and angles in [PO_4] and Ca coordination clusters. Therefore, the HA structure becomes disordered with a consequent high density of energy levels within the band gap, as demonstrated by the broad band model (Fig. 5c). In this sense, the equilibrium between structural order–disorder effects controls the radiative emissions of f-HA particles.

The understanding of the self-activated fluorescence phenomenon in HA particles and the optimization of the aforementioned defects responsible for the creation

of efficient luminescent centers are an ongoing research area with several studies found in the literature. For instance, in a pioneer experimental study, Aronov and colleagues [95] observed a very wide and continuous fluorescence emission and concluded through electronic trap states spectroscopy that a complex structure of electron/hole bulk and surface localized states are present in f-HA nanoceramics. In a study conducted by our research group [39], it was observed that an asymmetrical broad band emission (Fig. 6) with maxima of intensity centered at 445 and 470 nm ($\lambda_{exc} = 350$ nm) or 480 and 505 nm ($\lambda_{exc} = 415$ nm) was present in chemically precipitated HA with distinct particle shape, which were composed of five or seven individual emission components, respectively (Fig. S1 and Fig. S2 in Ref. [39]). The main difference between the emission profiles was in their intensities. This behavior was mainly attributed to the different concentrations of HPO_4^{2-}, V_{Ca}, V_{OH} vacancies, and atomic dislocations from their equilibrium positions, thus leading to distinct densities of localized energy states within the wide band gap of f-HA. Furthermore,

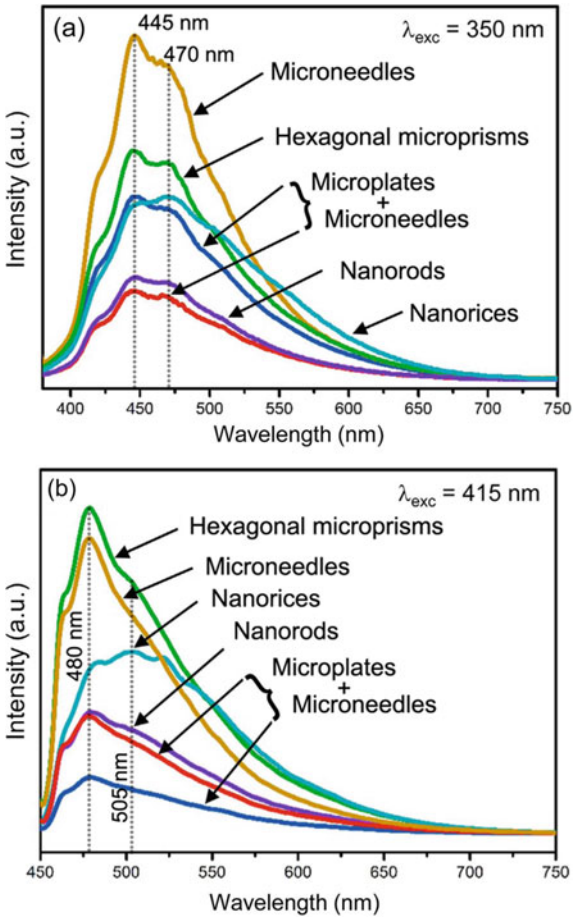

Fig. 6 Fluorescence emission spectra of f-HA particles with distinct sizes and shapes synthesized via chemical precipitation. **a** $\lambda_{exc} = 350$ nm, **b** $\lambda_{exc} = 415$ nm. The variations in emission intensity were mainly attributed to distinct densities of point and structural defects that caused changes in energy states within the wide band gap of f-HA. Reprinted with permission from Ref. [39]

the fluorescence spectra of rice-like f-HA nanoparticles were slightly red-shifted—a behavior that was assigned to the higher density of optically active defects on the surfaces and interfaces of the NPs resulting from their imperfect crystallization and attachment.

In a subsequent study, based on the results obtained by cathodoluminescence, photoluminescence and EPR experiments, Huerta and colleagues [79] suggested that V_{Ca}, V_{OH}, and V_O vacancies in PO_4 and OH groups, as well as $V_{OH} + H_i$ complex defect, perturb the electronic structure of f-HA synthesized by hydrothermal-assisted precipitation, being these defects the main responsible for the four individual components observed for the broad band fluorescence emission centered at 517 nm ($\lambda_{exc} =$ 325 nm). Similar emission profiles were obtained in Fe^{3+}-doped f-HA nanobelts with the general formula $Ca_{(10-3x)}Fe_{2x}(PO_4)_6(OH)_2$ prepared via an ion exchange procedure posterior to the hydrothermal-assisted precipitation [96]. A general increase in fluorescence intensity was observed in Fe^{3+} concentrations up to 12.05 at.%, a behavior that was mainly attributed to the formation of extra V_{Ca} vacancies generated by Fe^{3+} doping. On the other hand, Kumar and Girija [68] proposed that the emission of f-HA microflowers centered at 430 nm ($\lambda_{exc} = 344$ nm) may be due to luminescent centers of CO_3^{2-} and/or defects associated with this substituent.

When posterior thermal treatments are conducted in precipitated f-HA particles, several reactions encompassing the trapped impurities take place, changing the concentration and chemical nature of the point defects and profoundly impacting the structural long- and short-range order of the HA lattice [97]. It was reported that structural H_2O and NH_4^+ impurities are eliminated at temperatures up to ~400 °C, causing a significant decrease in lattice constants *a* and *c*, whereas CO_3^{2-} groups are decomposed and/or redistributed via several reactions located in the broad temperature range of 400–1200 °C, leading to distinct steps of increase in lattice parameter *a* [98]. At 500 °C, there is a partial filling of hexagonal channels with OH- groups, which is completed at 600–700 °C, suppressing V_{OH} vacancies.

Together with these temperature-dependent structural and compositional oscillations, the f-HA particles also show dramatic variations in the amplitude, intensity, and center position of their fluorescence emission profile. However, the optimal temperature to achieve the best fluorescence properties was found to be between 350 and 450 °C, which is after the elimination of most part of volatile impurities, with the consequent shrinkage of the crystalline lattice, and when the partial decomposition of CO_3^{2-} initiates, leading to an improved equilibrium between order–disorder effects and an optimized density of localized energy levels [60, 61]. For example, in this temperature range chemically precipitated f-HA nanorods exhibit very broad emission bands, where the maximum of emission shifts from 460 nm (untreated particles) to 535 nm at 350 °C when excited at $\lambda_{exc} = 350$ nm, as shown in Fig. 7a; in this case, the fluorescence emission becomes up to 11 times more intense when compared to the raw particles [37]. Additionally, the heat-treated f-HA nanoparticles exhibit multicolor property, causing them to display excitation-dependent emission spectra at $\lambda_{exc} =$ 330–680 nm due to the thermally-induced high density of defective levels within the band gap region (Fig. 7b). Some studies also pointed out that an important parameter for the fluorescence response of heat-treated f-HA is the initial content

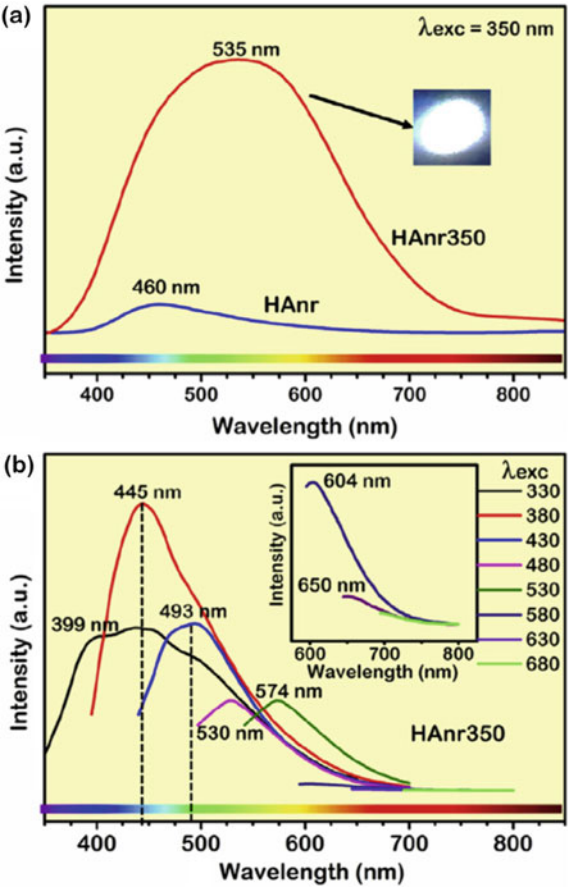

Fig. 7 **a** Photoluminescence emission spectra (λ_{exc} = 350 nm) of chemically precipitated f-HA nanorods (HAnr) and heat-treated f-HA nanorods at 350 °C/4 h, and **b** excitation-dependent photoluminescence emission spectra of f-HA nanorods heat-treated at 350 °C/4 h. Reprinted with permission from Ref. [37]

of CO_3^{2-} and the density of associated defects during the precipitation, leading to significant variations mainly in the intensity of the emission band in the temperature range of 350–450 °C [60, 99].

In the case of f-HA particles obtained by Cit^{3-}-based synthesis under hydrothermal conditions, the presence of carbon- and nitrogen-related impurities trapped in the HA lattice seems to play an important role in their fluorescence properties. Zhang and colleagues [71] anticipated that some R–C–COO^- units from Cit^{3-} suffer a bond cleavage under high pressure and temperature conditions, forming R–C• and $CO_2^{\bullet-}$ radicals. The latter paramagnetic radical species is then trapped in the HA lattice or interstitial positions, leading to a broad band emission centered at 428 nm (λ_{exc} = 341 nm) not observed in the HA sample obtained without the Cit^{3-} precursor, as shown in Fig. 8a,b. It was also indicated that the fluorescence intensity depends on the initial Cit^{3-}:Ca^{2+} molar ratio in f-HA (from 0:1 to 3:1) and the pH value established during synthesis [71, 72]. A similar explanation based on $CO_2^{\bullet-}$ radicals for the origin of the emission profile observed in f-SrHA particles

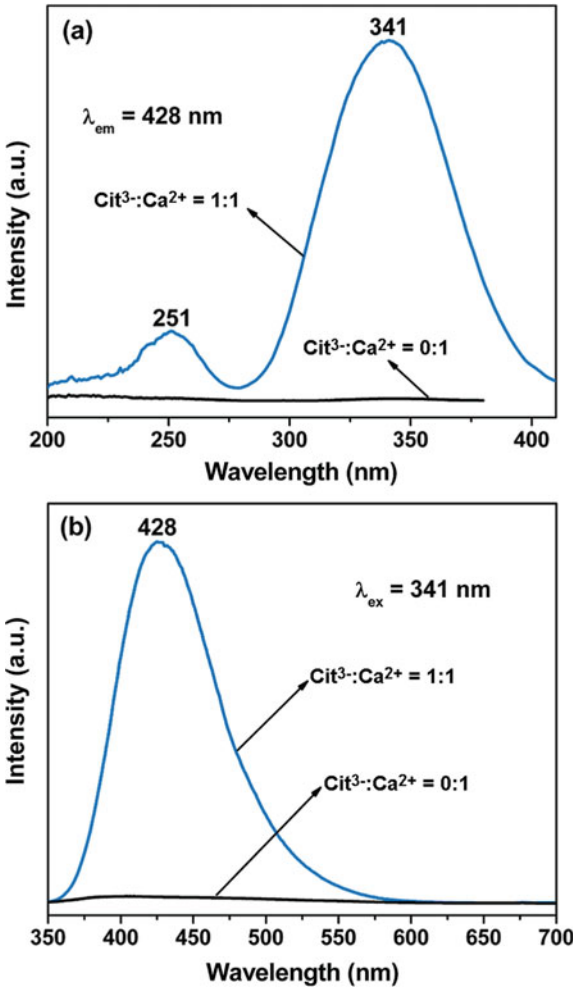

Fig. 8 **a** Photoluminescence excitation and **b** emission spectra of f-HA NPs obtained by hydrothermal-assisted precipitation in the presence of trisodium citrate precursor (blue line) and without trisodium citrate (black line). Reprinted with permission from Ref. [71]

was reported in Ref. [73]. Further studies demonstrated that the Sr^{2+}:(Ca^{2+} + Sr^{2+}) (from 0 to 1) and Cit^{3-}:Sr^{2+} (from 0:1 to 4:1) molar ratios also affect the fluorescence intensity of f-SrHA particles [83, 100].

However, Jiang and colleagues [74] presented experimental evidence that refuted the presence of $CO_2^{\bullet-}$ radicals in f-HA and proposed that the optically active defects are in fact amorphous and nanosized N-rich carbon dots (CDs) trapped in the f-HA lattice or in interstitial positions, thus acting as luminescent centers. As illustrated in Fig. 9, the N-rich CDs are formed under hydrothermal conditions as a product of both Cit^{3-} and NH_4^+ ions, that is, they originate from the precursors containing these ionic species. These findings were further reinforced by a recent study conducted by Cheng and colleagues [75], which used distinct mixtures of $(NH_4)_3PO_4{\cdot}3H_2O$/$Na_3PO_4{\cdot}12H_2O$ precursors to obtain f-HA NPs via Cit^{3-}-based

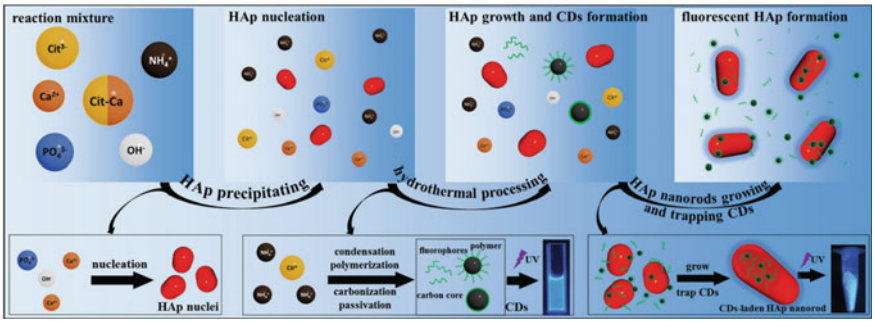

Fig. 9 Proposed formation mechanism for f-HA via Cit^{3-}-assisted hydrothermal treatment. When $(NH_4)_2HPO_4$ precursor solution is added, Ca^{2+} ions are released from the chelates formed between Ca^{2+} and Cit^{3-}, forming the first HA nuclei by the reaction with PO_4^{3-} and OH^- followed by crystal growth. Then, a reaction encompassing Cit^{3-} and NH_4^+ takes place, forming N-rich CDs containing fluorophore molecules, polymer clusters, and nanosized carbon cores. These cores are gradually trapped in the HA lattice and its interstices, leading to self-activated f-HA. Reprinted with permission from Ref. [74]

hydrothermal treatment. According to the authors, 50/50 or 100/0 mixtures can lead to rod-like NPs with superior colloidal stability and fluorescence emission intensity in comparison with solely $Na_3PO_4 \cdot 12H_2O$ precursor. Evidence of CDs as luminescent centers inside f-HA was also demonstrated by Wang and colleagues [77].

Table 1 summarizes the main features and mechanisms in HA particles for the occurrence of self-activated fluorescence according to the synthesis methodology and the experimental setup for the luminescence measurements. Depending on the preparation route and the initial precursors, the proposed defects present in f-HA can significantly change—a fact that guarantees the possible tuning of fluorescence properties in f-HA.

5 Applications

Fluorescent HA particles are widely explored for applications ranging from tissue engineering to bioimaging and theragnosis. For these purposes, the luminescent properties of HA-based systems can be tuned by several approaches, such as the encapsulation of organic fluorophores, the doping with luminescent ions, or the combination of HA and other luminescent materials [19]. On the other hand, the self-activated fluorescence has become a great alternative to improve the fluorescence properties of HA particles for various applications, which will be discussed in the next sections.

Table 1 Main experimental methodologies to obtain fluorescent HA particles

Material	Synthesis approach	Particle morphology	Excitation	Emission	Origins of fluorescence	Ref
f-HA	Chemical precipitation	Nanorods (50–60 nm × 12–25 nm) Nanorods (300–600 nm × 40–80 nm) Microplates and microneedles (0.5–5.5 μm × 0.03–0.2 mm) Prismatic microrods (0.7–2.5 μm × 0.07–0.2 mm)	λ_{exc} = 350 and 415 nm, krypton ion laser, 7 and 14 mW, respectively	Broad band emission centered between 445–505 nm, depending on the λ_{exc} and the particle size and shape	Structural order–disorder. Radiative recombination of e′–h• pairs in defect-related energy levels within the forbidden zone of HA as an effect of loss of symmetry in $[CaO_9]$, $[CaO_7H]$ and $[PO_4]$ clusters in bulk and surface. This effect stems mainly from crystal disorder and V_{Ca} and V_{OH} vacancies	[39]
f-HA	Chemical precipitation followed by heat treatment steps (200–800 °C)	Nanorods (300–600 nm × 40–80 nm)	λ_{exc} = 350/415 nm, 300–38 K, krypton ion laser, 7/14/30 mW, λ_{exc} = 330–630 nm, Xenon lamp, 450 W	Broad band emission centered between 399–650 nm, depending on the excitation wavelength and source as well as the heat treatment (200–800 °C) and temperature of analysis	Structural order–disorder as in [39]. The thermally-induced elimination or decomposition of trapped impurities (H_2O, CO_3^{2-} and NH_4^+) from the HA lattice intensifies the radiative recombination of e′–h• pairs in defect-related energy levels	[37, 61]

(continued)

Table 1 (continued)

Material	Synthesis approach	Particle morphology	Excitation	Emission	Origins of fluorescence	Ref
f-HA	Chemical precipitation using eggshell precursor	Nanorods (~50 nm × 20 nm)	λ_{exc} = 405 nm, pump laser	Broad band emission centered at 515 nm. Emission intensity dependent on the heat treatment temperature (400–900 °C) and pH (7–9) during synthesis	CO_3^{2-} luminescent centers substituting PO_4^{3-} groups (B-type) in the HA lattice	[69]
f-HA f-SrHA	Hydrothermal-assisted precipitation	Nanorods 50–70 nm × 25 nm (pH = 9) 120–150 nm × 20 nm (pH = 7) Microspheres 7–9 μm (pH = 5) 10 μm (pH = 4.5)	λ_{exc} = 345 nm, Xenon lamp, 150 W	Broad band emission centered at 432 nm. Lifetime = 11.6 ns, quantum yield = 22%. Emission intensity dependent on the Cit^{3-}/Sr^{2+} molar ratio	$CO_2^{\bullet-}$ luminescent centers trapped in the f-HA and f-SrHA lattices and originated from Cit^{3-}	[71, 73]
f-HA	Hydrothermal-assisted precipitation	Nanorods (30–200 nm × 20–30 nm)	λ_{exc} = 300–370 nm, Xenon lamp, 150 W	Broad band emission centered between 427–442 nm, depending on the λ_{exc}. Lifetime = 4.36 ns. Quantum yield = 31.43%	N-rich carbon dot luminescent centers trapped in the HA lattice and originated from Cit^{3-} and NH_4^+ ions	[74]
f-HA	Hydrothermal-assisted precipitation	Nanobelts (0.5–3.0 μm × 10–50 nm)	λ_{exc} = 325 nm, He-Cd laser	Broad band emission centered at 517 nm	V_O vacancy from PO_4^{3-} or OH, V_{OH}, V_{Ca}, and $V_{OH} + H_i$ vacancies	[79]

(continued)

Table 1 (continued)

Material	Synthesis approach	Particle morphology	Excitation	Emission	Origins of fluorescence	Ref
f-HA	Sol–gel method	Nanorods (92.8 nm × 23.2 nm) Short nanorods (35 nm × 7 nm) Thin nanorods (62.5 nm × 6.2 nm)	$\lambda_{exc} = 325$ nm, He-Cd laser, 300–15 K;	Broad band emission centered between 502–528 nm, depending on the temperature of analysis. Intensity dependent on the aspect ratio of NPs	Confinement of free electrons in an asymmetric potential created by the elongated shape of NPs with discrete optically active superficial energy levels	[81]

5.1 Plain Fluorescence Imaging

Fluorescence imaging is a versatile, non-invasive and low-cost technique with high sensitivity and selectivity that allows the capture of images with high contrast, being potentially used in nanomedicine as a powerful diagnosis tool [101]. Deshmukh and colleagues [81] used f-HA nanorods (62.5 nm × 6.2 nm) obtained by the sol–gel method for in vitro plain fluorescence imaging. The f-HA NPs exhibited a blue fluorescence (maximum at 502 nm, $\lambda_{exc} = 325$ nm) stable in phosphate-buffered saline (PBS, pH 7) solution and in Dulbecco's modified Eagle's medium (DMEM). The NPs were well-internalized by both prokaryotic and eukaryotic cells, leading to green and red fluorescence inside the cells, as observed with the aid of an epifluorescence microscope using TRITC and FITC filters (Fig. 10). At dosages up to 1000 $\mu g.mL^{-1}$, the f-HA nanorods displayed a nonhemolytic and low cytotoxic behavior, as determined by MTT and LDH assays, without any significant ROS generation.

Mostly, the application of f-HA NPs is conducted by their excitation in the near-ultraviolet region, which ends up limiting their applicability in deeper tissues due to the high absorption of light by hemoglobin and water. Therefore, it is interesting to use excitation wavelengths closer to the biological window (~650–900 nm), where light has enhanced depth of penetration in tissues [102]. In a recent work, it was demonstrated the multicolor cell imaging capability of f-HA nanorods obtained by chemical precipitation followed by heat treatment at 350 °C/4 h [37]. Using HDFn cells as a model, the internalized f-HA NPs in the cytosol region evidenced the cellular structure by fluorescence emission in confocal microscopy at $\lambda_{exc} = 405$, 488, 543 and 594 nm, leading to blue, green, yellow and red colors, respectively. Also, no interference was observed by the co-labeling of cytoskeleton with fluorescein and no evident cytotoxicity was found up to 320 $\mu g.mL^{-1}$ of NPs.

The self-activated fluorescence of HA can be also combined with other luminescent species in order to tune its fluorescence emission. Wang and colleagues prepared Tb^{3+}-doped f-HA nanorods (51.1 ± 9.7 nm in length) with bright green fluorescence and low cytotoxicity by Cit^{3-}-assisted precipitation under hydrothermal treatment [77]. The fluorescence was stable for 72 h in SBF and H_2O, and a high internalization and labeling capabilities ($\lambda_{exc} = 488$ nm) in C6 cell cytoplasm was verified by the conjugation of transferrin receptor on the NPs surfaces.

5.2 Fluorescence-Guided Therapy

Since the 1970s, HA has been identified as an efficient system for the transfection of genes applied in the treatment of various pathologies [18]. Currently, CaPs are considered promising pH-responsive nanocarriers for the targeted delivery of distinct bioactive compounds to tumor sites, being widely used in chemotherapy, gene therapy, photodynamic therapy, hyperthermia therapy, and so on [17, 19]. The combination of fluorescent imaging and therapy functions provided by HA represent

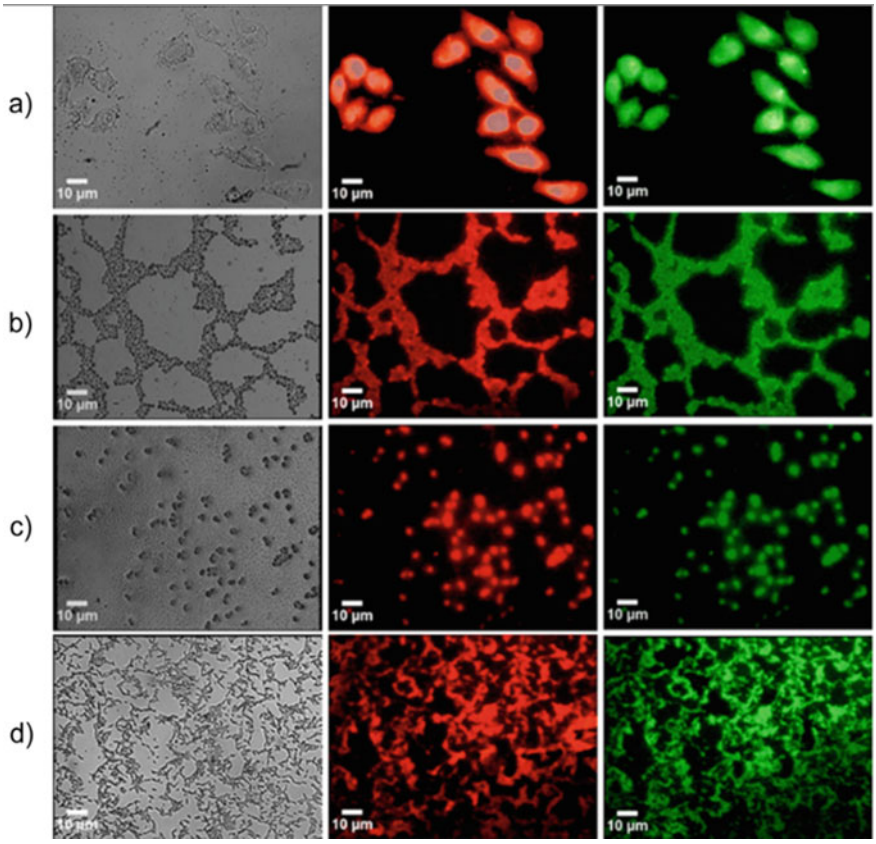

Fig. 10 Epifluorescence microscopy images of cells containing uptaken f-HA nanorods synthesized via a modified sol–gel procedure using bright field *(left)*, FITC filter *(center)* and TRITC filter *(right)*, evidencing the bright green and red emissions of f-HA inside the cells. **a** HeLa cells, **b** *Candida albicans*, **c** *Staphylococcus aureus*, **d** *Escherichia coli*. Reprinted with permission from Ref. [81]

the state-of-the-art of nanomedicine and allows the development of efficient theranostic nanoplataforms with several successfully reported strategies via in vitro and in vivo probes [103].

The f-HA particles can deliver a large variety of bioactive molecules, and the drug loading and release can be monitored by their self-activated fluorescence property. It was shown that the f-HA flower-like nanostructures obtained by eggshell can be loaded with doxycycline hydrochloride (28.3% of loading efficiency), reaching an initial burst release of about 60% for 6 h followed by a slow release of 8% for 54 h, consequently leading to an antibacterial activity against *E. coli* and *B. cereus* [68]. Zhang and colleagues [100] utilized mesoporous f-SrHA nanorods for the delivery of ibuprofen, and demonstrated a loading efficiency of 32.9% and a total drug release of 50.5% after 3 h and 93.9% after 12 h. The ibuprofen-loaded f-SrHA NPs showed

strong blue fluorescence at 432 nm with a continuous increase in emission intensity during drug release, allowing its monitoring. A quenching of luminescent centers by vancomycin loading (efficiency of 16.58%) in mesoporous f-SrHA microflowers was observed by Jiang and colleagues [83], who reported that the cumulative amount of released drug molecules can also be monitored by the emission band centered at 432 nm. In another study, Park and collaborators [80] achieved a higher loading efficiency of 59.1% of vancomycin in f-SrHA microspheres, with a fast release in the first 6 h through the breakage of the hydrogen bonding of vancomycin molecules on the outer surface of the f-SrHAP particle followed by the saturation of drug release after 72 h, as shown in Fig. 11.

To increase the drug loading capability of f-HA particles, they can be combined with mSi. Yang and colleagues [82] used spherical mSi@f-HA NPs (200–400 nm) comprised of a crystalline f-HA layer and an amorphous-mesoporous SiO_2 core to monitor the delivery of captopril. These NPs expressed a loading capability of 33.7%,

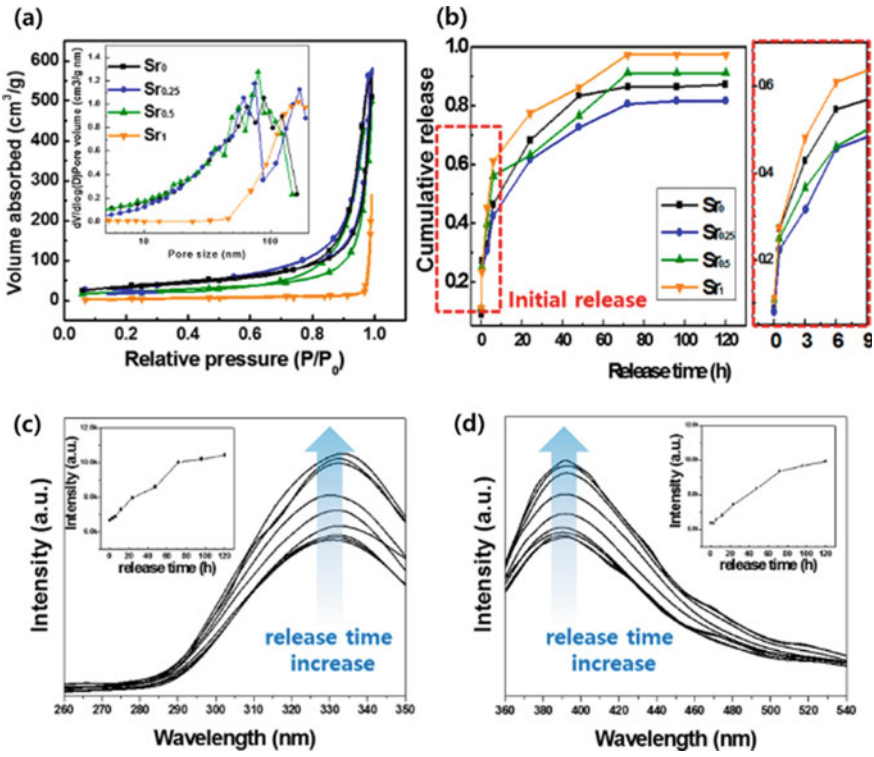

Fig. 11 **a** N_2 adsorption–desorption isotherm and pore size distributions (inset) of f-SrHA microspheres obtained by hydrothermal treatment, **b** cumulative release of vancomycin from f-SrHA in PBS, and **c, d** Photoluminescence excitation ($\lambda_{em} = 395$ nm) and emission ($\lambda_{exc} = 335$ nm) spectra of f-SrHA as a function of vancomycin release time. Reprinted with permission from Ref. [80]

and the captopril release was accompanied by variations in the intensity of blue emission at 410 nm. In another approach, Singh et al. [85] prepared f-HA@mSi nanorods functionalized with amino groups and comprised of a uniform layer of amorphous SiO_2. The loading capability of fluorescein isothiocyanate (FITC) increased from 1 μg for f-HA nanorods to a maximum of 10 μg for f-HA@mSiO_2 nanorods. The f-HA@mSiO_2 nanorods exhibited self-activated blue fluorescescence coexisting with FITC green intracellular signals, demonstrating the in situ imaging ability of the NPs with an uptake efficiency up to 93% in MC3T3-E1 cells. Furthermore, Singh and colleagues [72] covered mSi nanospheres (~200–300 nm) with f-HA nanorods (40 nm × 10 nm) and loaded them with small interfering RNA (siRNA) encoding Plekho-1. The nanocarrier showed a sustainable release over 5 days, an osteoblastic uptake of 96%, and a gene-silencing effect, suppressing Plekho-1 to 18.2%, whereas the self-activated blue fluorescence was used to image the intracellular nanocarrier.

The f-HA particles can also be combined with other contrast agents for multimodal imaging-guided therapy. Li and colleagues [78] prepared Gd^{3+}-doped f-SrHA nanorods coated with aptamers, which acted both as capping and targeting agents for the controlled release of doxorubicin (DOX) into breast cancer cells (MCF-7). Since DOX molecules quenched the self-activated blue fluorescence of Gd^{3+}-doped f-SrHA nanorods, it was inferred that the increase in emission intensity can be used to monitor the targeted drug release process inside high-level nucleolin expressed MCF-7 cells. In addition, the blue fluorescence and T1-weighted bright contrast from Gd^{3+} dopant make these NPs an ideal candidate for both targeted multimodal imaging and therapy.

5.3 Biosensing

Fluorescence-based detection is widely applied in biosensing approaches given its high sensitivity, simplicity, and diversity. Moreover, fluorescence sensing based on NPs is an exciting research area with various possibilities of application in biology and medicine due to the superior luminescent properties of the NPs. Specifically, f-HA NPs are biocompatible and can be tailored to have a large surface area in order to immobilize different biomolecules. For instance, a selective in vitro testing of protein kinase A (PKA) activity was conducted by fluorescence using f-HA nanorods, as demonstrated by an assay with HeLa cell lysates [104]. The detection was made by PKA-catalyzed phosphorylation of a peptide substrate, where the resulting phosphopeptides bound to f-HA, quenching its self-activated blue fluorescence. In this specific case, the PKA concentrations in the 1–50 $U.L^{-1}$ range were successfully correlated with f-HA fluorescence intensity, and a detection limit of 0.5 $U.L^{-1}$ was achieved.

In another approach, a fluorescence assay using f-HA nanorods was developed for the selective detection of alkaline phosphatase (ALP) activity in the human serum [76]. Initially, the fluorescence of f-HA was quenched by the addition of Cu^{2+} ions. Then, pyrophosphate ions were introduced to restore the fluorescence intensity of the

NPs due to the formation of a complex between these groups and Cu^{2+} ions. When ALP molecules were added to the reaction assay, the hydrolysis of pyrophosphate groups took place, leading to another quenching effect caused by Cu^{2+} ions and making ALP detectable in the range of 1–625 $U.L^{-1}$.

5.4 Bone Treatment and Regeneration

Self-activated blue luminescence of f-HA nanorods (100 nm) can be utilized as a tool to examine the intracellular molecular mechanism of osteogenesis of bone mesenchymal stem cells (BMSCs) promoted by PO_4^{3-} ions, aiming at the development of treatment procedures for bone metabolic diseases [105]. The f-HA NPs can be incorporated into cells via macropinocytosis pathway to the lysosome vesicle that degrades the nanorods due to the acidic pH environment inside the vesicle, thus releasing PO_4^{3-} ions (Fig. 12). This latter process is accompanied by the decrease in intensity of HA fluorescence as the particles are dissolved in the 3–48 h interval, as observed by intracellular imaging. Then, the PO_4^{3-} ions from f-HA nanorods facilitate the differentiation of BMSCs into osteoblasts by mediating the adenosine-triphosphate (ATP) synthesis in the mitochondria—a process that induces

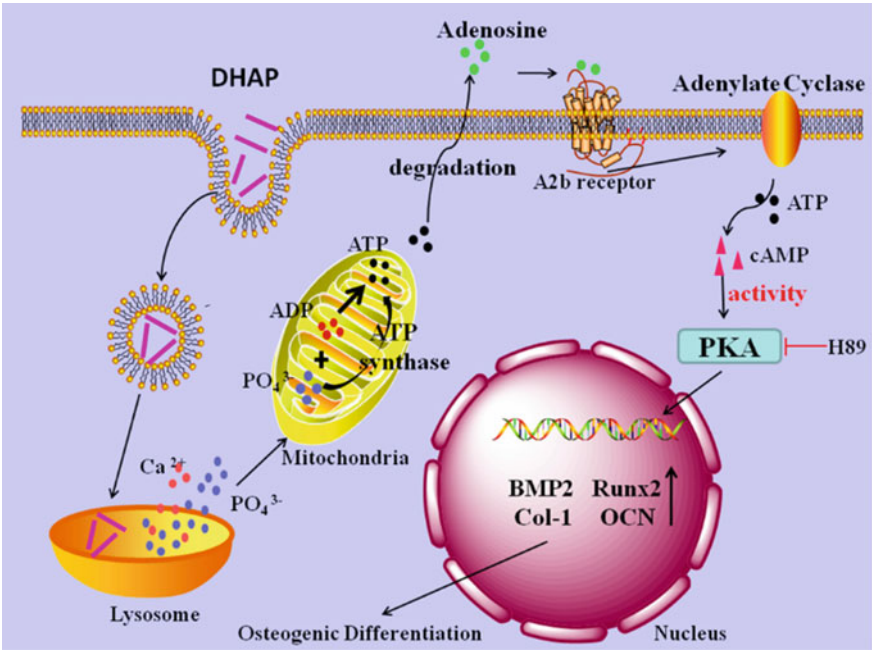

Fig. 12 Contribution of f-HA nanorods to the osteogenic differentiation of BMSCs. Reprinted with permission from Ref. [105]

the cAMP/PKA pathway—consequently leading to the high mRNA expression of osteogenic differentiation-related genes.

In another study, the self-activated blue luminescence was used to investigate the bone regeneration pathways promoted by f-HA nanorods [106]. It was demonstrated that the NPs can be uptaken by osteoblasts via caveolae-mediated endocytosis and micropinocytosis. Furthermore, these NPs were located in lysosomes, as determined by the intracellular fluorescence signal departing from the NPs. The authors concluded that the f-HA NPs promoted bone regeneration through both intracellular and extracellular pathways. For instance, the intracellular f-HA NPs upregulated the OCN gene expression in the osteoblast cells, the synthesis of collagen and the formation of mineralized nodules, whereas the extracellular f-HA NPs acted as nucleation sites for mineralized nodules, as determined by their blue fluorescence.

Moreover, the preparation of f-HA NPs containing molybdenum oxides (MoO_x) was also reported, exhibiting antibacterial activity for application in bone repair as real-time imaging platforms against bone infection [107].

5.5 Other Applications

f-HA nanorods exhibiting strong defect-related blueish- and yellowish-white emission were considered possible candidates for the fabrication of low-cost and non-toxic light-emitting diodes (LEDs) [61]. On the other hand, Cheng and colleagues obtained f-HA nanorods with excellent colloidal stability, and proposed their utilization for long-term storage of confidential information and anti-counterfeit printing [75]. Dispersions of f-HA NPs were used to make inks for infiltration, writing, and printing on commercial paper, showing no background fluorescence. As shown in Fig. 13, the information can be easily observed using a portable UV lamp—but not by the naked eye under natural light. Other applications that take advantage of the fluorescence properties of HA include the characterization of HA-based photocatalysts [41], the structural and compositional changes in bones [108, 109], and early caries detection [69].

6 Conclusions and Perspectives

The study of self-activated fluorescence in HA micro- and nanoparticles is an ongoing research topic that has attracted the attention of scientists from various areas with several methodologies available in the current literature. Depending on the synthesis methodology by wet approaches, such as chemical precipitation, hydrothermal-assisted precipitation, **s**ynthesis from natural bio-resources and sol–gel method, as well as the correct choice of synthesis parameters and the nature of the precursor compounds, the main features of the fluorescence (i.e., emission color, intensity, and emission band amplitude) can be significantly changed and greatly enhanced. Thus,

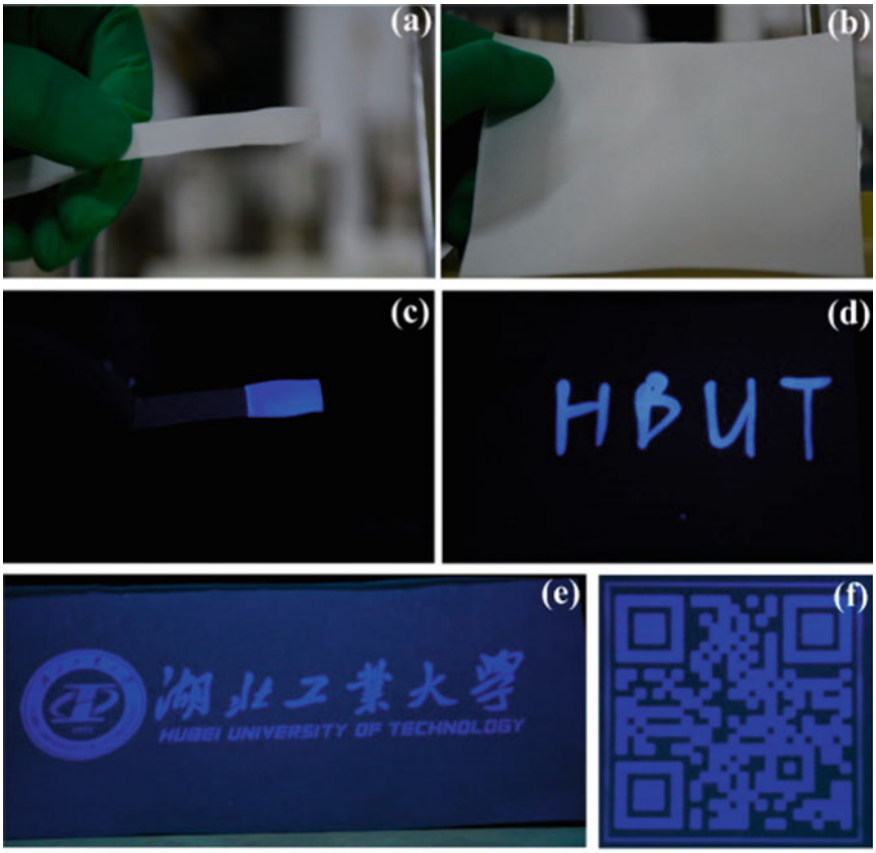

Fig. 13 Photograph of paper infiltrated with f-HA under **a** natural light, **b** $\lambda_{exc} = 365$ nm. Photograph of written paper using f-HA under **c** natural light, **d** $\lambda_{exc} = 365$ nm. Photograph of printed paper using f-HA under $\lambda_{exc} = 365$ nm evidencing **e** Chinese and English characters, **f** QR code. Reprinted with permission from Ref. [75]

it is essential to have a fine control and optimization of the preparation route in order to obtain improved and reproducible fluorescent properties in f-HA. In this sense, the joint theoretical and experimental approaches can lead to new insights into the main defects that can be manipulated so as to achieve the desirable properties in f-HA.

HA is one of the most interesting materials explored in a vast list of applications, ranging from bone/tooth repair and tissue engineering to bioimaging, biosensing, drug delivery, gene therapy and theranostics. Among the various advantages of HA for these purposes, e.g., biocompatibility, bioactivity, and the capability to load and delivery several biomolecules, its superior structural flexibility is a remarkable feature since the HA crystalline structure accepts distinct foreign substituents, ionic vacancies, interstitials and structural distortions without collapsing. One important effect

of this characteristic is the possibility of stabilizing several defects that act as luminescent centers, leading to self-activated broad band fluorescence in HA particles in the near-UV and visible regions despite the wide optical band gap of HA. The presence of auto-fluorescence properties allows the preparation of f-HA particles by less expensive and complicated approaches while enabling larger possibilities of sophisticated applications in technological and nanomedicine fields. Overall, f-HA particles exhibit good prospects for use in biological applications, being of particular interest. However, considering the wide range of complex compositions, f-HA still needs to be further studied in order to clarify some aspects that are not well-understood and improve its potential for application in large-scale treatments. We strongly believe that this review will be very useful for researchers working in various branches of science and engineering, such as physics, chemistry, materials science, and chemical engineering.

Acknowledgements The authors acknowledge the financial support of the following agencies: Conselho Nacional de Desenvolvimento Científico e Tecnológico (CNPq, Grants 164373/2020-9 and 141964/2018-9), and Fundação de Amparo à Pesquisa do Estado de São Paulo (FAPESP, Grant 2013/07296-2). Juan Andres acknowledges Universitat Jaume I for project UJI-B2019-30, and Ministerio de Ciencia, Innovacion y Universidades (Spain) project PGC2018- 094417-B-I00 for supporting this research financially.

References

1. Dorozhkin, S.V., Epple, M.: Angew. Chem. Int. Ed. **41**, 3130 (2002)
2. DileepKumar, V.G., Sridhar, M.S., Aramwit, P., Krut'ko, V.K., Musskaya, O.N., Glazov, I.E., Reddy, N.: J. Biomater. Sci. Polym. Ed. **33**, 229 (2022)
3. Chen, I.-H., Lee, T.-M., Huang, C.-L.: Gels **7**, 31 (2021)
4. Wang, L., Nancollas, G.H.: Chem. Rev. **108**, 4628 (2008)
5. Dessì, M., Alvarez-Perez, M.A., De Santis, R., Ginebra, M.P., Planell, J.A., Ambrosio, L.: J. Mater. Sci. Mater. Med. **25**, 283 (2014)
6. Arcos, D., Vallet-Regí, M.: J. Mater. Chem. B **8**, 1781 (2020)
7. Shepherd, J.H., Shepherd, D.V., Best, S.M.: 2335 (2012)
8. Lee, D.W., Kim, J.Y., Lew, D.H.: J. Craniofac. Surg. **21**, 1084 (2010)
9. Zhou, H., Lee, J.: Acta Biomater. **7**, 2769 (2011)
10. Cho, J.-H., Garino, J.P., Choo, S.-K., Han, K.-Y., Kim, J.-H., Oh, H.-K.: Clin. Orthop. Surg. **2**, 214 (2010)
11. Choudhury, P., Agrawal, D.C.: Surf. Coatings Technol. **206**, 360 (2011)
12. Wang, M.: Biomaterials **24**, 2133 (2003)
13. Neacsu, I.A., Stoica, A.E., Vasile, B.S., Andronescu, E.: Nanomaterials **9** (2019)
14. Syamchand, S.S., Sony, G.: Microchim. Acta **182**, 1567 (2015)
15. Cai, A.Y., Zhu, Y.J., Qi, C.: Adv. Mater. Interf. **7**, 1 (2020)
16. Khalifehzadeh, R., Arami, H.: Adv. Colloid Interf. Sci. **279**, 102157 (2020)
17. Haider, A., Haider, S., Han, S.S., Kang, I.K.: RSC Adv. **7**, 7442 (2017)
18. Uskoković, V., Uskoković, D.P.: J. Biomed. Mater. Res. - Part B Appl. Biomater. **96 B** 152 (2011)
19. Qi, C., Lin, J., Fu, L.H., Huang, P.: Chem. Soc. Rev. **47**, 357 (2018)
20. Doat, A., Fanjul, M., Pellé, F., Hollande, E., Lebugle, A.: Biomaterials **24**, 3365 (2003)

21. Mondéjar, S.P., Kovtun, A., Epple, M.: J. Mater. Chem. **17**, 4153 (2007)
22. Li, L., Liu, Y., Tao, J., Zhang, M., Pan, H., Xu, X., Tang, R.: J. Phys. Chem. C **112**, 12219 (2008)
23. Yang, P., Quan, Z., Li, C., Kang, X., Lian, H., Lin, J.: Biomaterials **29**, 4341 (2008)
24. Chen, F., Huang, P., Zhu, Y.J., Wu, J., Zhang, C.L., Cui, D.X.: Biomaterials **32**, 9031 (2011)
25. Hui, J., Zhang, X., Zhang, Z., Wang, S., Tao, L., Wei, Y., Wang, X.: Nanoscale **4**, 6967 (2012)
26. Zheng, X., Liu, M., Hui, J., Fan, D., Ma, H., Zhang, X., Wang, Y., Wei, Y.: Phys. Chem. Chem. Phys. **17**, 20301 (2015)
27. Xie, Y., He, W., Li, F., Perera, T.S.H., Gan, L., Han, Y., Wang, X., Li, S., Dai, H., Appl, A.C.S.: Mater. Interf. **8**, 10212 (2016)
28. Ignjatović, N.L., Mančić, L., Vuković, M., Stojanović, Z., Nikolić, M.G., Škapin, S., Jovanović, S., Veselinović, L., Uskoković, V., Lazić, S., Marković, S., Lazarević, M.M., Uskoković, D.P.: Sci. Rep. **9**, 1 (2019)
29. Tabaković, A., Kester, M., Adair, J.H.: Wiley Interdiscip. Rev. Nanomed. NanoBiotechnol. **4**, 96 (2012)
30. Liu, H., Chen, F., Xi, P., Chen, B., Huang, L., Cheng, J., Shao, C., Wang, J., Bai, D., Zeng, Z.: J. Phys. Chem. C **115**, 18538 (2011)
31. Williams, R.L., Hadley, M.J., Jiang, P.J., Rowson, N.A., Mendes, P.M., Rappoport, J.Z., Grover, L.M.: J. Mater. Chem. B **1**, 4370 (2013)
32. Haedicke, K., Kozlova, D., Gräfe, S., Teichgräber, U., Epple, M., Hilger, I.: Acta Biomater. **14**, 197 (2015)
33. Guo, Y., Shi, D., Lian, J., Dong, Z., Wang, W., Cho, H., Liu, G., Wang, L., Ewing, R.C.: Nanotechnology **19** (2008)
34. Zhao, Y., Shi, L., Fang, J., Feng, X.: Nanoscale **7**, 20033 (2015)
35. Liu, M., Liu, H., Sun, S., Li, X., Zhou, Y., Hou, Z., Lin, J.: Langmuir **30**, 1176 (2014)
36. Ma, B., Zhang, S., Liu, R., Qiu, J., Zhao, L., Wang, S., Li, J., Sang, Y., Jiang, H., Liu, H.: Nanoscale **9**, 2162 (2017)
37. Machado, T.R., Leite, I.S., Inada, N.M., Li, M.S., da Silva, J.S., Andrés, J., Beltrán-Mir, H., Cordoncillo, E., Longo, E.: Mater. Today Chem. **14**, 100211 (2019)
38. Lyons, J.L., Janotti, A., Van De Walle, C.G.: Phys. Rev. Lett. **108** (2012)
39. Machado, T.R., Sczancoski, J.C., Beltrán-Mir, H., Li, M.S., Andrés, J., Cordoncillo, E., Leite, E., Longo, E.: Ceram. Int. **44**, 236 (2018)
40. Slepko, A., Demkov, A.A.: Phys. Rev. B - Condens. Matter Mater. Phys. **84**, 1 (2011)
41. Bystrov, V.S., Piccirillo, C., Tobaldi, D.M., Castro, P.M.L., Coutinho, J., Kopyl, S., Pullar, R.C.: Appl. Catal. B Environ. **196**, 100 (2016)
42. Matsunaga, K., Kuwabara, A.: Phys. Rev. B - Condens. Matter Mater. Phys. **75**, 1 (2007)
43. Anicete-Santos, M., Silva, M.S., Orhan, E., Góes, M.S., Zaghete, M.A., Paiva-Santos, C.O., Pizani, P.S., Cilense, M., Varela, J.A., Longo, E.: J. Lumin. **127**, 689 (2007)
44. Ikoma, T., Yamazaki, A., Nakamura, S., Akao, M.: Netsu Sokutei **25**, 141 (1998)
45. Narasaraju, T.S.B., Phebe, D.E.: J. Mater. Sci. **31**, 1 (1996)
46. Uskoković, V.: RSC Adv. **5**, 36614 (2015)
47. Kay, M.I., Young, R.A., Posner, A.S.: Nature **204**, 1050 (1964)
48. Boanini, E., Gazzano, M., Bigi, A.: Acta Biomater. **6**, 1882 (2010)
49. Lu, X., Zhang, H., Guo, Y., Wang, Y., Ge, X., Leng, Y., Watari, F.: Cryst. Eng. Commun. **13**, 3741 (2011)
50. Bee, S., Hamid, Z.A.A.: Ceram. Int. 1 (2020)
51. Wopenka, B., Pasteris, J.D.: Mater. Sci. Eng. C **25**, 131 (2005)
52. Peroos, S., Du, Z., De Leeuw, N.H.: Biomaterials **27**, 2150 (2006)
53. Fleet, M.: Carbonated Hydroxyapatite: Materials, Synthesis, and Applications, 1st edn. Pan Stanford Publishing, New York (2015)
54. Elliot, J.C.: Structure and Chemistry of the Apatites and Other Calcium Orthophosphates, 1st edn. Elsevier Publisher, Ammsterdam (1994)
55. Tite, T., Popa, A.C., Balescu, L.M., Bogdan, I.M., Pasuk, I., Ferreira, J.M.F., Stan, G.E.: Materials (Basel) **11**, 1 (2018)

56. Sadat-Shojai, M., Khorasani, M.T., Dinpanah-Khoshdargi, E., Jamshidi, A.: Acta Biomater. **9**, 7591 (2013)
57. Liu, C., Huang, Y., Shen, W., Cui, J.: Biomaterials **22**, 301 (2001)
58. Rodríguez-Lorenzo, L.M., Vallet-Regí, M.: Chem. Mater. **12**, 2460 (2000)
59. Shavandi, A., Bekhit, A.E.D.A., Sun, Z., Ali, A., Biomimetics, J.: Biomater. Biomed. Eng. **25**, 98 (2015)
60. Gonzalez, G., Costa-Vera, C., Borrero, L.J., Soto, D., Lozada, L., Chango, J.I., Diaz, J.C., Lascano, L.: J. Lumin. **195**, 385 (2018)
61. Machado, T.R., Sczancoski, J.C., Beltrán-Mir, H., Nogueira, I.C., Li, M.S., Andrés, J., Cordoncillo, E., Longo, E.: J. Solid State Chem. **249**, 64 (2017)
62. Zollfrank, C., Müller, L., Greil, P., Müller, F.A.: Acta Biomater. **1**, 663 (2005)
63. Arul, K.T., Kolanthai, E., Manikandan, E., Bhalerao, G.M., Chandra, V.S., Ramya, J.R., Mudali, U.K., Nair, K.G.M., Kalkura, S.N.: Mater. Res. Bull. **67**, 55 (2015)
64. Mahabole, M.P., Bahir, M.M., Kalyankar, N.V., Khairnar, R.S.: J. Biomed. Sci. Eng. **05**, 396 (2012)
65. Arul, K.T., Ramya, J.R., Karthikeyan, K.R., Kalkura, S.N.: Mater. Lett. **135**, 191 (2014)
66. Soares Da Silva, J., Machado, T.R., Martins, T.A., Assis, M., Foggi, C.C., MacEdo, N.G., Beltrán-Mir, H., Cordoncillo, E., Andrés, J., Longo, E.: Inorg. Chem. **58**, 5900 (2019)
67. Figueroa-Rosales, E.X., Martínez-Juárez, J., García-Díaz, E., Hernández-Cruz, D., Sabinas-Hernández, S.A., Robles-Águila, M.J.: Curr. Comput.-Aided Drug Des. **11**, 832 (2021)
68. Kumar, G.S., Girija, E.K.: Ceram. Int. **39**, 8293 (2013)
69. Goloshchapov, D.L., Minakov, D.A., Domashevskaya, E.P., Seredin, P.V.: Results Phys. **7**, 3853 (2017)
70. Sinha, A., Pal, A., Murmu, A.S.S., Amit, U.K.G., Chowdhury, R.: J. Inst. Eng. Ser. D (2020)
71. Zhang, C., Yang, J., Quan, Z., Yang, P., Li, C., Hou, Z., Lin, J.: Cryst. Growth Des. **9**, 2725 (2009)
72. Singh, R.K., Kim, T.H., Patel, K.D., Kim, J.J., Kim, H.W.: J. Mater. Chem. B **2**, 2039 (2014)
73. Zhang, C., Cheng, Z., Yang, P., Xu, Z., Peng, C., Li, G., Lin, J.: Langmuir **25**, 13591 (2009)
74. Jiang, D., Zhao, H., Yang, Y., Zhu, Y., Chen, X., Sun, J., Yu, K., Fan, H., Zhang, X.: J. Mater. Chem. B **5**, 3749 (2017)
75. Cheng, C., Tong, K., Fang, Y., Wang, J., Liu, Y., Tan, J.: Coatings **9**, 1 (2019)
76. Yang, W., Luo, J., Qi, M., Yang, M.: Anal. Methods **11**, 2272 (2019)
77. Wang, C., Jeong, K.-J., Kim, J., Kang, S.W., Kang, J., Han, I.H., Lee, I.-W., Oh, S.-J., Lee, J.: J. Colloid Interf. Sci. **581**, 21 (2021)
78. Li, Z., Liu, Z., Yin, M., Yang, X., Yuan, Q., Ren, J., Qu, X.: Biomacromol **13**, 4257 (2012)
79. Huerta, V.J., Fernández, P., Gómez, V., Graeve, O.A., Herrera, M.: Appl. Mater. Today **21**, 100822 (2020)
80. Park, S.Y., Il Kim, K., Park, S.P., Lee, J.H., Jung, H.S.: Cryst. Growth Des. **16**, 4318 (2016)
81. Deshmukh, K., Shaik, M.M., Ramanan, S.R., Kowshik, M., Biomater, A.C.S.: Sci. Eng. **2**, 1257 (2016)
82. Yang, P., Yang, P., Teng, X., Lin, J., Huang, L.: J. Mater. Chem. **21**, 5505 (2011)
83. Jiang, F., Wang, D.P., Ye, S., Zhao, X.: J. Mater. Sci. Mater. Med. **25**, 391 (2014)
84. Rodríguez-Ruiz, I., Delgado-López, J.M., Durán-Olivencia, M.A., Iafisco, M., Tampieri, A., Colangelo, D., Prat, M., Gómez-Morales, J.: Langmuir **29**, 8213 (2013)
85. Singh, R.K., Kim, T.-H., Patel, K.D., Mahapatra, C., Dashnyam, K., Kang, M.S., Kim, H.-W.: J. Am. Ceram. Soc. **97**, 3071 (2014)
86. Rulis, P., Ouyang, L., Ching, W.Y.: Phys. Rev. B - Condens. Matter Mater. Phys. **70**, 1 (2004)
87. Bhat, S.S., Waghmare, U.V., Ramamurty, U.: Cryst. Growth Des. **14**, 3131 (2014)
88. Jiménez-Flores, Y., Suárez-Quezada, M., Rojas-Trigos, J.B., Lartundo-Rojas, L., Suárez, V., Mantilla, A.: J. Mater. Sci. **52**, 9990 (2017)
89. De Leeuw, N.H.: J. Mater. Chem. **20**, 5376 (2010)
90. Matsunaga, K.: Phys. Rev. B - Condens. Matter Mater. Phys. **77**, 1 (2008)
91. Bystrov, V.S., Coutinho, J., Bystrova, A.V., Dekhtyar, Y.D., Pullar, R.C., Poronin, A., Palcevskis, E., Dindune, A., Alkan, B., Durucan, C., Paramonova, E.V.: J. Phys. D. Appl. Phys. **48**, 195302 (2015)

92. Bystrova, A.V., Dekhtyar, Y.D., Popov, A.I., Coutinho, J., Bystrov, V.S.: Ferroelectrics **475**, 135 (2015)
93. Bystrov, V.S., Avakyan, L.A., Paramonova, E.V., Coutinho, J.: J. Phys. Chem. C **123**, 4856 (2019)
94. Pasteris, J.D., Wopenka, B., Freeman, J.J., Rogers, K., Valsami-Jones, E., Van Der Houwen, J.A.M., Silva, M.J.: Biomaterials **25**, 229 (2004)
95. Aronov, D., Chaikina, M., Haddad, J., Karlov, A., Mezinskis, G., Oster, L., Pavlovska, I., Rosenman, G.: J. Mater. Sci. Mater. Med. **18**, 865 (2007)
96. Carrera, K., Huerta, V., Orozco, V., Matutes, J., Fernández, P., Graeve, O.A., Herrera, M.: Mater. Sci. Eng. B Solid-State Mater. Adv. Technol. **271**, (2021)
97. Tõnsuaadu, K., Gross, K.A., Pluduma, L., Veiderma, M.: J. Therm. Anal. Calorim. **110**, 647 (2012)
98. Zyman, Z.Z., Rokhmistrov, D.V., Glushko, V.I., Ivanov, I.G.: J. Mater. Sci. Mater. Med. **20**, 1389 (2009)
99. Goloshchapov, D.L., Seredin, P.V., Minakov, D.A., Domashevskaya, E.P.: Opt. Spectrosc. (English Transl. Opt. i Spektrosk. **124**, 187 (2018)
100. Zhang, C., Li, C., Huang, S., Hou, Z., Cheng, Z., Yang, P., Peng, C., Lin, J.: Biomaterials **31**, 3374 (2010)
101. Wolfbeis, O.S.: Chem. Soc. Rev. **44**, 4743 (2015)
102. Weissleder, R.: Nat. Biotechnol. **19**, 316 (2001)
103. Degli Esposti, L., Carella, F., Adamiano, A., Tampieri, A., Iafisco, M.: Drug Dev. Ind. Pharm. **44**, 1223 (2018)
104. Zhang, K., Zeng, K., Shen, C., Tian, S., Yang, M.: Microchim. Acta **185** (2018)
105. Wang, C., Liu, D., Zhang, C., Sun, J., Feng, W., Liang, X.J., Wang, S., Zhang, J.: ACS Appl. Mater. Interf. **8**, 11262 (2016)
106. Dai, C., Zhu, L., Chen, G., Haddleton, D.M.: RSC Adv. **9**, 35939 (2019)
107. Placente, D., Ruso, J.M., Baldini, M., Laiuppa, J.A., Sieben, J.M., Santillán, G.E., Messina, P.V.: Nanoscale **11**, 17277 (2019)
108. Lambrecht, G., Mallol, C.: J. Archaeol. Sci. Reports **31**, 102333 (2020)
109. Sandri, A., Basso, P.R., Corridori, I., Protasoni, M., Segalla, G., Raspanti, M., Spinelli, A.E., Boschi, F.: J. Biophotonics **14**, 1 (2021)